UNIVERSITY OF CALIFORNIA, SAN DIEGO

Spines of the Porcupine Fish: Structure, Composition, and Mechanical Properties

A Thesis submitted in partial satisfaction of the requirements

for the degree Master of Science

in

Materials Science and Engineering

by

Frances Yenan Su

Committee in Charge:

Professor Joanna M. McKittrick, Chair
Professor Vlado A. Lubarda
Professor Jan B. Talbot

2015

The Thesis of Frances Yenan Su is approved and it is acceptable in quality and form for publication on microfilm and electronically:

Chair

University of California, San Diego

2015

Table of Contents

List of Figures

List of Tables

Acknowledgements

I would like to acknowledge Professor Joanna McKittrick for her support as the chair of my committee, and for intellectually stimulating discussions about the porcupine fish spine.

I would also like to acknowledge the contributions of the following individuals and groups who have helped in immeasurable ways: Professor Philip Hastings and H.J. Walker of the Scripps Institution of Oceanography for generously providing me with fish samples for testing from their extensive specimen collection; Professor Vlado Lubarda for providing valuable insight into the methods of deriving of mechanical models for this thesis, as well as for being one of my committee members; Dr. Eric Bushong, Tom Deerinck, Andrea Thor, and Professor Mark Ellisman from the National Center for Microscopy and Imaging at UC San Diego for assisting me with techniques for imaging biological materials as well as performing nano-CT with my samples; Kyungah Seo, Dr. Katya Novitskaya, and Professor Olivia Graeve for performing TGA and XRD with my samples; Steven Herrera and Professor David Kisailus from UC Riverside for helping me with nanoindentation tests, and Esther Cory and Professor Robert Sah for performing micro-CT on my fish specimen.

Finally, I would like to thank my fellow lab members for their insightful comments and expertise in experimental methods.

ABSTRACT OF THE THESIS

Spines of the Porcupine Fish:

Structure, Composition, and Mechanical Properties

by

Frances Yenan Su

Master of Science in Materials Science and Engineering

University of California, San Diego, 2015

Professor Joanna M. McKittrick, Chair

This thesis explores the structure, composition, and mechanical properties of the porcupine fish spine for the first time. The spine was found to be composed of nanocrystalline hydroxyapatite and protein that is most likely mainly type I collagen using X-ray diffraction, energy-dispersive X-ray spectroscopy, and thermogravimetric analysis. Microstructure that includes mineralized fiber sheets in the longitudinal direction and radial orientation of the sheets in the transverse direction were observed using light microscopy and electron microscopy. Mechanical properties were calculated

using nanoindentation and a cantilever beam test. Finally a tapered cantilever beam model was developed and compared to that of a uniform cantilever beam. The tapered beam model showed that while the stresses experienced were similar, the location of the maximums stress in the beam is near the tip of the beam rather than the base.

1 Introduction

Spines are stiff tapered structures that protrude from an organism and can be found in mammals (e.g. porcupine, echidna, etc.), plants (e.g. cacti, roses, etc.) insects, reptiles, birds, echinoderms, and fish. While spines can be used offensively, for instance in bees and wasps, many organisms use spine structures as a form of defense. Organisms that use spines for defense include porcupines, hedgehogs, cacti, and sea urchins. Spines are used to deter predators by piercing and irritating predators. This introduction will introduce the differences in materials and structures of different spines found throughout a diverse range of organisms across the planet.

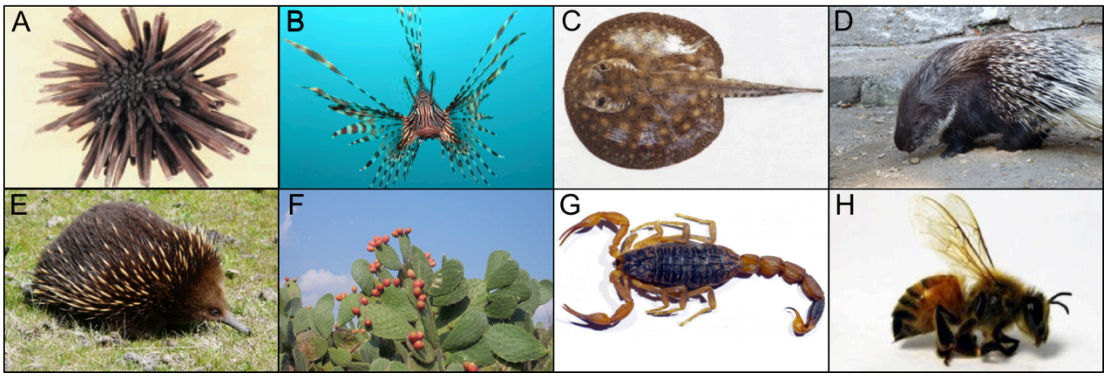

Figure 1. Various organisms with spine structures. **(a)** Sea urchin [1], **(b)** lionfish [2], **(c)** stingray [3], **(d)** porcupine [4], **(e)** echidna [5], **(f)** cactus [6], **(g)** scorpion [7], and **(h)** honey bee [8]. Figures are adapted from cited sources.

Spine structures can be made of a variety of biological materials. Sea urchin **(**Figure 1a**)** spines are composed of single crystal magnesium calcite with the crystallographic c-axis oriented longitudinally with the length of the spine [9, 10]. Lionfish **(**Figure 1b**)** dorsal spines are made of dentine, which is a composite of hydroxyapatite and collagen [11-13]. Stingray **(**Figure 1c**)** stings are also composed of

dentine [14, 15]. Spines and quills found in hedgehogs, porcupines **(**Figure 1d**)**, and echidnas **(**Figure 1e**)** are made of keratin and are believed to have evolved from hair [16, 17]. Cactus **(**Figure 1f**)** spines are made almost equal parts of crystalline cellulose and amorphous hemicellulose, both of which are polysaccharides [18, 19]. Meanwhile, scorpion **(**Figure 1g**)**, bee **(**Figure 1h**)**, and wasp stingers are made of chitosan, which is also a polysaccharide [7, 8]. Structures and mechanical properties of different spines are described in Table 1.

Table 1. Summary of animal spine composition, structure, and mechanical properties.

Animal Spine	Composition	Structure	E(GPa)	σ_f (MPa)	References
Sea Urchin	Calcite	• Highly-oriented magnesium calcite crystals • Triangular or rectangular cross-section • Concentric rings of calcite	 ^{T} 58.6 (n) ^{L} 64-65 (n) 22 (b)	13-41 (b) 48 (c)	[1] [20] [9] [10]
Sting Ray	Calcium Phosphate	• Flattened cross-section • Serrated edges • Covered in venom			[3]
Lionfish	Calcium Phosphate	• Slender and straight for most of length and tapers at end			[11]
Porcupine	Keratin	• Cylindrical with tapered end • Old World porcupines have radial symmetry in transverse cross-section • New World porcupines: Foam-like infill	5.56-6.05	0.712 (b) 63-170 (c)	[17] [21]
Hedgehog	Keratin	• Cylindrical with proximal bulbous end • Radial symmetry in transverse direction	11.56 Wet 2.3 (t) Dry 3.8 (t)	2.44 (b)	[17]
Cactus	Cellulose	• Highly aligned cellulose microfibrils parallel to spine axis	17.4 (t) Green 28 (b) Dry 33.5 (b) 1-12.7 (t)	140 (t) Green 609 (b) Dry 779 (b) 84-93.3 (t)	[22] [19] [18, 19]
Bee	Chitosan	• Compose of three hollow components that can move relative to each other • Barbed near tapered tip			[8]
Wasp	Chitosan	• Flattened, tapered, tube structure • Barbed near tapered tip • Reinforcing piece to prevent buckling			[8]
Scorpion	Chitosan	• Hollow, tapered, and curved rod • Laminated microstructure of oriented chitin fibrils	0.8-1.8 (n)		[7]
(t) = tensile test results, (b) = bending test results, (c) = compression test results, nanoindentation (n), ^{T} = transverse direction, ^{L} = longitudinal direction					

Spine structures have a variety of internal structures depending on their other functions. Hedgehogs, old world porcupines, and sea urchins all have material alignment in the radial direction (first row of Figure 2). Both the lionfish and sea urchin spines incorporate cyclic, concentric magnesium into the structure in the transverse direction [9]. The chitosan based structures of the honey bee, paper wasp, and scorpion have a hollow tube structure (second row of Figure 2). The internal structure of the cactus and Old World porcupine are cellular (third row of Figure 2).

It is important to note the multifunctionality that is intrinsic to biological materials. Spines can be useful to an organism for a variety of reasons. For example, in addition to protection, the cactus uses its spines, which are modified leaves, to prevent water loss in its native desert habitat. Hedgehogs use their quills to not only deter predators, but also to absorb energy when they fall from high places [17]. The lionfish, stingray, bee, wasp, and scorpion all use venom to supplement their stings, but the structures of their stingers are quite different. The lionfish and stingray stings have venom glands that line the sides of the spine, while in bee, wasp, and scorpion stings venom flows through the stingers.

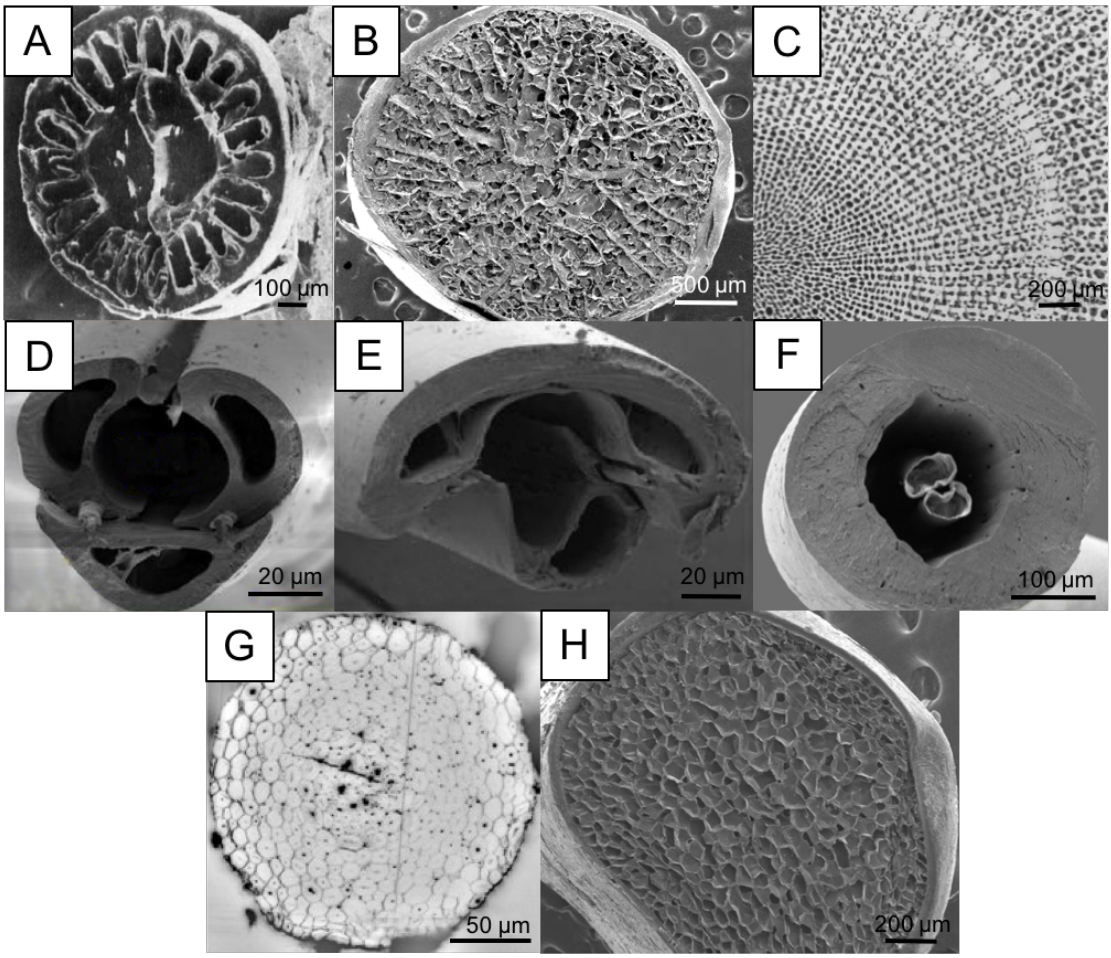

Figure 2**.** Cross-sections of various spine structures found in nature: **(a)** hedgehog spine [17], **(b)** Old World porcupine quill [21], **(c)** sea urchin spine [1], **(d)** honey bee sting [8], **(e)** paper wasp sting [8], **(f)** scorpion sting [7], **(g)** cactus spine [19], **(h)** New World porcupine quill [23].

2 Background

2.1 General Information and Life Cycle

Porcupine fish belong to a unique family within the order Tetraodontiformes called *Diodontidae* [24]. While the order Tetradontiformes is an extremely diverse group that includes the boxfish and triggerfishes, the porcupine fish is most closely related to the families *Tetraodontidae* and *Molidae*, which include pufferfish and ocean sunfish, respectively [24]. Porcupine fish are characterized by their ability to inflate, as well as their long spines that become erect when threatened. Leis [25] divides the family *Diodon* into two groups: The slender-bodied group, which consists of the *D. eydouxii* and *D. hystrix,* and the round-bodied group, which includes *D. holocanthus*, *D. liturosus,* and *D. nicthemerus* (all shown in Figure 3). The two species used in this study are the round-bodied *D. holocanthus* and the slender-bodied *D. hystrix*.

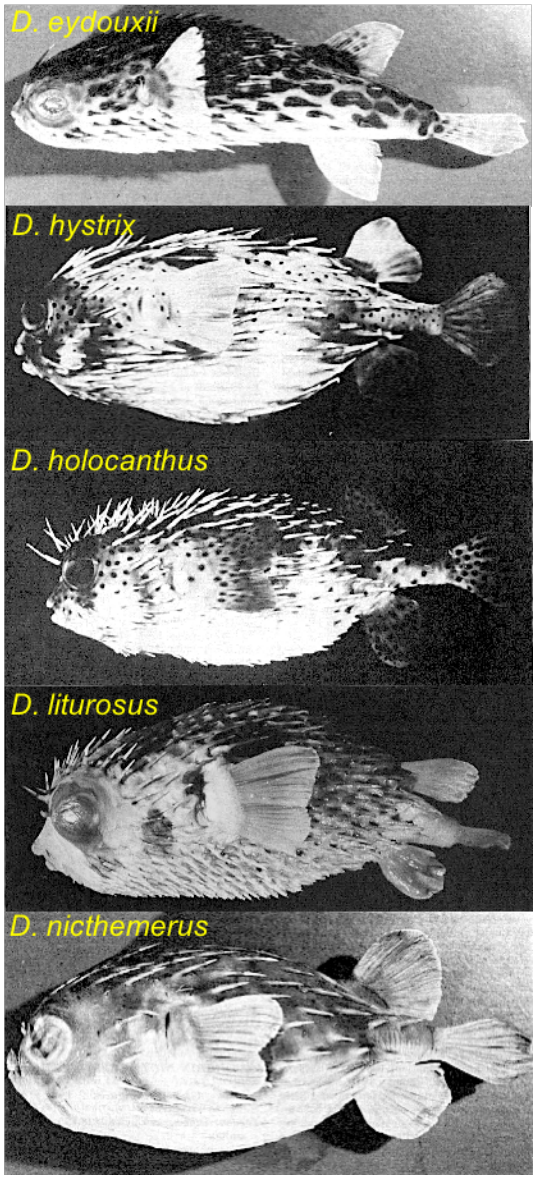

Figure 3. Fish from the family *Diodon*: from top to bottom, *D. eydouxii*, *D. hystrix*, *D. holocanthus*, *D. liturosus*, and *D. nicthemerus*. Figure adapted from Leis [25].

Porcupine fish are found in tropical and temperate marine waters and feed on hard-shelled invertebrates [25, 26]. The following life cycle of the porcupine fish consists of four stages: egg, larval, juvenile, and adult [25]. The eggs and larvae are pelagic, meaning that they live near the surface of the ocean and away from land [25]. Metamorphosis to the juvenile stage occurs when the porcupine fish reaches about 3-5

mm in length and lasts for an unknown amount of time. Juveniles are characterized by the spines that develop on the body [25]. Adults separate themselves from juveniles through the body proportions. Spines elongate and the body becomes more elliptical. For the *D. holocanthus* the pigment changes and results in the formation of spots on the belly of the fish. Porcupine fish can live up to 10 years and the largest sample recorded had a length of 90 cm [25]. They are also commonly kept as pets in saltwater aquariums.

Porcupine fish are nocturnal predators that feed on mollusks and shellfish. Their strong teeth can crack mollusk shells [25]. These teeth are one of the characteristic traits of the order Tetraodontiformes and form a beak-like structure that is actually multiple teeth fused together. These teeth continually grow, so it is important for them to feed on shelled animals to grind their teeth down.

2.2 Porcupine Fish Defense Mechanisms

During the egg and larval stages, plankton feeders eat porcupine fish. Juveniles are preyed upon by pelagic predators including tuna, dolphinfish, and wahoo [27]. Once porcupine fish reach the adult stage the number of predators decreases significantly, because the fish becomes too large swallow. The main predator of the adult porcupine fish is the tiger shark, which appears to be immune to the toxin (discussed in Section 2.2.2) that porcupine fish produce.

2.2.1 Inflation

Porcupine fish, like their pufferfish relatives from the family Tetraodontidae, can inflate their bodies up to three times their original volume when threatened [28]. It is believed that the inflation mechanism developed from coughing, which is present in

almost all fish, to water-blowing that is found in certain species in the tetraodontiformes order, and finally to inflation [29]. This progression is shown in a phylogenic tree in Figure 4.

During inflation, water or air is pumped into the stomach. Breder, et al. [30] stated (as cited from Brainerd [28]) that the stomach function has been divided into the dorsal "inflatable sac," and the ventral "stomach proper." Inflation is also an energy intensive process that fatigues the fish if done too many times in a short time period. Brainerd [28] found that porcupine fish could no longer inflate after inflating 5-8 times in short succession.

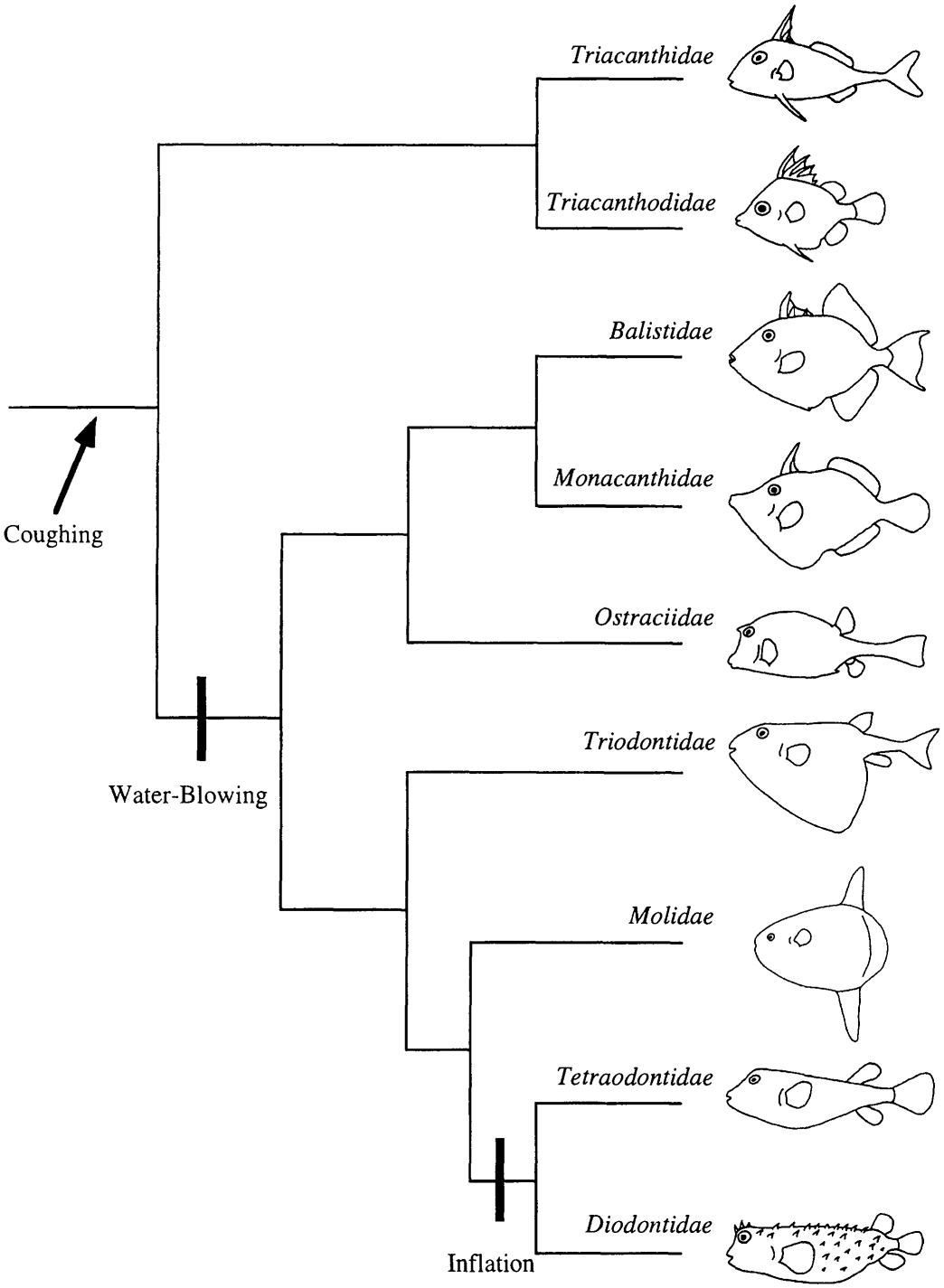

Figure 4. Phylogeny of the order Tetraodontiformes with hypothesized progression of inflation evolution [24, 29, 31].

2.2.2 Toxin

In addition, members of the family *Diodontidae* and *Tetraodontidae* can be poisonous and contain a toxin called tetraodotoxin. The toxin is mainly found in the ovaries and liver of pufferfish [32], but can also be found in the skin of some puffers [33]. Tetrodotoxin has also been found in newts in the family *Salamandridae* [34, 35] as well as shellfish, starfish, and the blue-ringed octopus [32]. Mines, et al. [36] argue that tetrodotoxin, rather than being a metabolic byproduct, is actually produced by bacteria ingested by the fish from food sources such as starfish. There are three main reasons why this may be true: 1) Tetrodotoxin is found in such a wide variety of organisms that it is unlikely that its production evolved independently so many times, 2) laboratory raised porcupine fish and newts do not produce the toxin [32], and 3) common marine bacteria from the genus *Vibrio* have been found to be part of pufferfish microflora [37] and have been proven to produce tetrodotoxin [38]. Sugita, et al. [37] also found that the bacteria population depends on the temperature of the water that pufferfish live in, which may explain why the amount of toxin in the fish can vary based on the season [32] and habitat.

Tetraodotoxin has been studied extensively, because it is an amino perhydroquinazoline, a compound that binds to the surface of voltage gated sodium ion channels. This prevents the voltage threshold necessary for sensory and motor signal propagation from being reached or extends the time it takes to reach the threshold [39]. Tetrodotoxin has been studied as a compound with potential to alleviate symptoms of heroin withdrawal [40] and painful conditions such as neuralgia and gastralgia [33].

The first signs of tetrodotoxin poisoning to exhibit themselves are tingling sensation in the mouth, nausea, and dizziness [36, 39]. Later symptoms include weakness,

numbness, and impaired speech [36, 39]. Excess salivation and sweating has also been observed [35]. If severely poisoned, symptoms progress to impaired breathing, bradycardia, and hypotension [36, 39]. Symptoms normally manifest themselves anywhere from 15 minutes to hours after ingestion of tetrodotoxin, depending on the amount of toxin ingested [36].

The fatality rate is approximately 50% for those who ingest the toxin, and those who survive the first 24 hours have a good chance at recovery [32]. Since there is no antidote for tetrodotoxin, recommended treatment is symptom-based and usually includes cardiorespiratory support [33, 39].

2.2.3 Spines

Despite the fact that tetrodotoxin is fatal to many organisms, porcupine fish are still preyed on by sharks and other marine predators. In addition to inflating their bodies, porcupine fish also have long spines across their body that are erectile when the fish inflates [26]. These spines serve to increase the effective volume of the porcupine fish, making it harder for predators to swallow, and are actually modified scales [26, 41, 42]. Leis [26]counted the number of spines in certain regions of members of the Diodon family and then counted the number of rows of spines on other areas of the body. The *D. hystrix* has approximately 29-38 spines from the snout to dorsal fin base (S-D) and from the lower jaw to the anus (S-A). In addition, between the pectoral fins over the dorsum (P-D-P) there are 15 rows of spines, and between the pectoral fins over the ventrum of the fish (P-V-P), there are 25 rows of spines. For the D. holocanthus, there are 12-16 S-D spines, 12-15 S-A spines, 11 rows of P-D-P spines, and 24 rows of P-V-P spines.

Apart from general observations, little to no work has been done on the composition and microstructure of the porcupine fish spine. However some work has been done to understand the spine structure and potential function of puffers in the family Tetraodontidae, which are closely related to porcupine fish. Hertwig, et al. [43] observed that the dermal spines in*Tetraodon steindachneri* have bilateral symmetry and have a laminated longitudinal cross-section. The spines of the *T. steindachneri* and *Takifugu obscurus* can be stained using alizarin red-S (Figure 5), a histological dye that indicates the presence of calcium [41, 43]. Of note, spines have a dense outer layer of collagen around the mineralized core [43], as well as many concentric circles in the transverse cross-section of the spines [41].

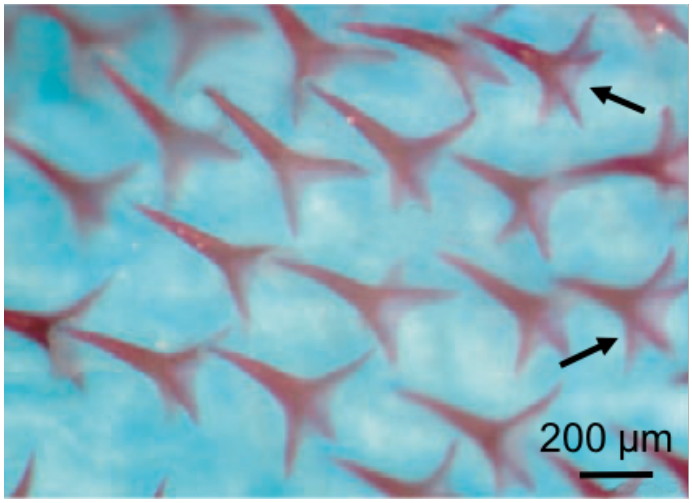

Figure 5. Fugu **(***Takifugu obscurus)* spines in larvae stained with alizarin red-S, which indicates the presence of calcium. Arrows point at spines with more than two lateral processes. Figure adapted from [41].

The composition of porcupine fish spines is largely unknown, since alizarin red only signifies the presence of calcium but does not specify whether the spines contain calcium carbonate, hydroxyapatitite, or both minerals. However, since spines are modified scales, it can be expected that the composition of porcupine fish spines should

be similar to that of other fish scales. In general, many scales are composed of highly aligned type I collagen, hydroxyapatite, and in some cases, calcium carbonate [44, 45]. Sire, et al. [46] note that the dermal plates in tetraodontiformes are composed of only bone. However, the order tetraodontiformes is so diverse in morphology that it is unlikely that every modified scale across the order is compositionally identical.

In the porcupine fish, Brainerd [28] identified three different regions of the spine shown in Figure 6: the spinous process, the lateral processes, and the axial process. Leis [25] refers to these regions as the spine shaft, the lateral arms of the base, and shaft extension, respectively. Spines generally have bilateral symmetry with two lateral processes, one spinous process, and one axial process. However, Leis [25] notes that there can be more than two lateral processes. This can also be seen in the *T. obscurus* spines (Figure 5).

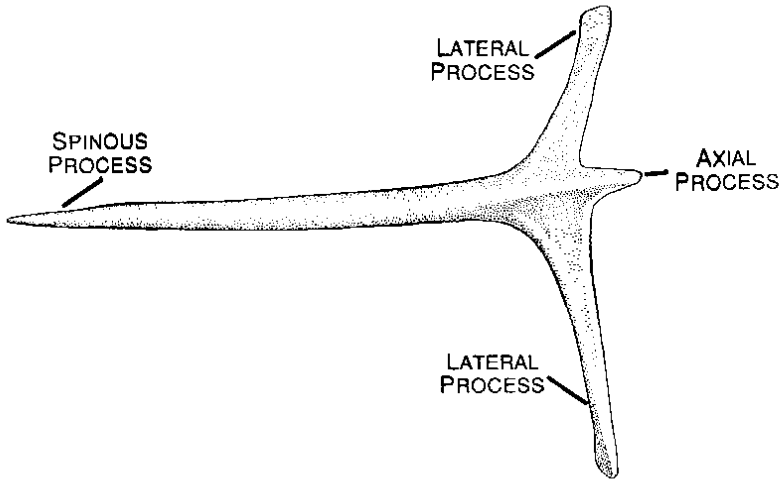

Figure 6. Porcupine fish spine drawing from Brainerd [28]. The lateral processes and axial process are embedded in the skin of the porcupine fish, while the spinous process extends out of the body of the fish.

3 Hypothesis

This thesis aims to characterize the composition, structure and mechanical properties of the porcupine fish spine. The spines of the porcupine fish, which are modified scales, must be able to withstand the force of a predator's jaw in order to not break. Therefore there are two main hypotheses this thesis aims to prove:

(I) The composition of the spines will be similar to that of other scales, meaning that the spines will most likely contain collagen and hydroxyapatite.

(II) The morphology and microstructure of the spines helps prevent the spine from failing.

4 Materials and Methods

One of each *D. holocanthus* (Museum ID: SIO 65-679) and *D. hystrix* (Museum ID: SIO H52-415) were received from the Scripps Institution of Oceanography. Samples had been fixed with 10% formalin and post-fixed in 50% isopropyl alcohol and deionized water. Spines were extracted from the right lateral side of the fish using a scalpel and surgical scissors to cut away skin and other connective tissue until the spine could be pried loose. Individual spines were stored in 50% isopropyl alcohol and deionized water.

4.1 X-ray Diffraction

For X-ray diffraction (XRD), one spine sample of *D. hystrix* was deproteinized by placing sample in 2.6% sodium hypochlorite solution for two days. Sample was then split into sections A, B, and C as shown in Figure 7 and ground to a powder using a mortar

and pestle. XRD was then performed on the sample powders using a Bruker D2 Phaser XRD (Bruker, Billerica, MA, USA) with 0.15406 nm wavelength. Sample analysis was done using DIFFRACplus software (Bruker, Billerica, MA, USA).

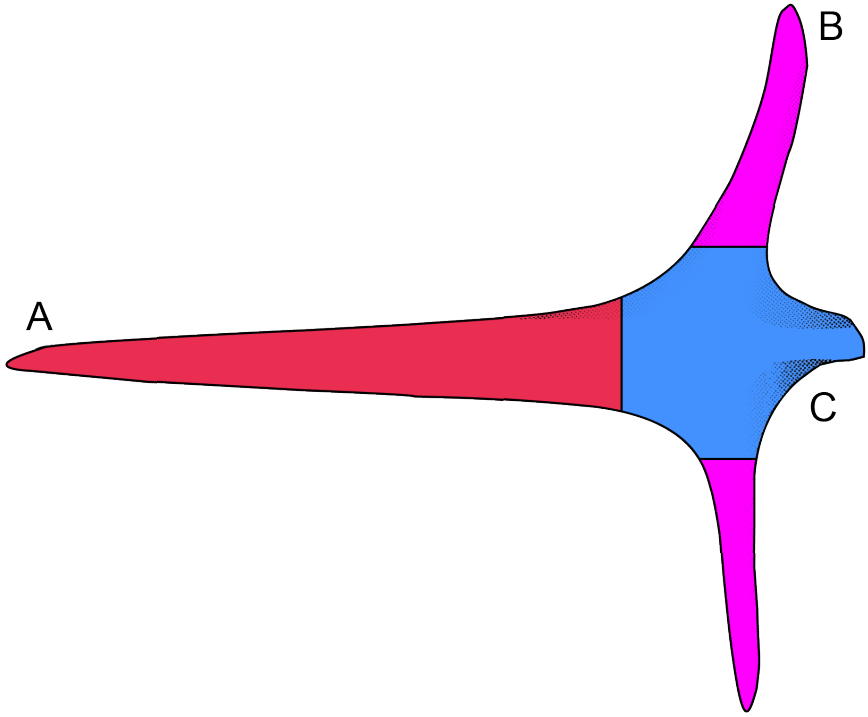

Figure 7. Colorized porcupine fish spine where A is the spinous process (red), B are the two lateral processes (pink), and C is the spine base (blue), which includes the axial process and the connection between sections A and B.

4.1.1 X-ray Diffraction Analysis

XRD patterns were matched using standard data from a PDF card. Crystallite size was found using the Scherrer equation

$$D = \frac{0.94\lambda}{\beta\ cos\theta} \tag{4.1}$$

where D is the average crystallite size, λ is the X-ray wavelength, β is the full width at half of the maximum intensity, and θ is the Bragg angle. Three of the peaks with highest

intensity were used to calculate average crystallite size. These values were then averaged to find a better approximation of crystallite size.

4.2 Thermogravimetric Analysis

Six samples of *D. holocanthus* spines prepared for thermogravimetric analysis (TGA) were first step-wise rehydrated by putting samples in solutions of 25%, 12.5%, and 0% isopropyl alcohol and deionized water for 10 minutes in each solution. Samples were then put in deionized water again and left overnight. Samples were cut into three sections A, B, and C (Figure 7), and were dabbed with a tissue to remove excess water before testing. Samples were then heated in the SDT Q600 Simultaneous TGA/DSC (TA Instruments, New Castle, DE, USA) from room temperature to 800˚C at a rate of 10˚C/min in air. All calculated values are given as mean ± standard deviation.

4.2.1 Data Analysis

Values of mass were taken from the temperature closest to those given by Bigi, et al. [47] and described in Section 5.3. Percentage of mass lost was calculated by dividing leftover mass by original mass of the sample.

4.3 Micro-Computed Tomography & Nano-Computed Tomography

For micro-computed tomography (μ-CT) the whole *D. holocanthus* sample was kept in a jar of 50% isopropyl alcohol and deionized water and imaged using a Skyscan 1076 μ-CT scanner (Bruker microCT, Kontich, Belgium) with a voxel size of 12.56 μm. Spine samples for nano-computed tomography (nano-CT) were first rehydrated, stained with osmium tetroxide, dehydrated, and embedded in Spurrs resin (protocol for sample

preparation in Appendix C). Spurrs resin was used because of its low viscosity and ability to infiltrate mineralized samples better than other resins. Samples were then imaged with Xradia 510 Versa (ZEISS, Jena, Germany). μ-CT and nano-CT results were processed using Amira® (FEI, Oregon, USA).

4.4 Scanning Electron Microscopy and Energy Dispersive X-Ray Spectroscopy

D. hystrix spines were step-wise dehydrated with 75%, 90%, 95%, and 100% isopropyl alcohol for 10 minutes each. Samples were then critical point dried using an Autosamdri-815 critical point dryer (tousimis, Rockville, MD, USA) (protocol described in Appendix C) or chemically dried using hexamethyldisilazane (HMDS) (protocol described in Appendix E). Samples were sputter coated with iridium at 85μA for 7 seconds to reduce charging using an Emitech K575X Sputter Coater (Quorum Technologies Ltd, East Sussex, UK). Spines were then imaged using an FEI/Philips XL-30 Environmental Scanning Electron Microscope (FEI, Hillsboro, OR, USA). Energy Dispersive X-Ray Spectroscopy was performed using an FEI SFEG ultra-high resolution scanning electron microscope (FEI, Hillsboro, OR, USA).

4.5 Histology and Transmission Electron Microscopy

Spine samples used for histology were first rehydrated and stained with osmium tetroxide. After staining, samples were washed and rehydrated with deionized water. Samples were then embedded in Spurrs resin using the protocol described in Appendix C. For histology and transmission electron microscopy (TEM), spines were sectioned using a Leica Ultracut UCT Ultramicrotome (Leica Microsystems, Wetzlar, Germany) into 250

nm slices and 80 nm slices, respectively. Histology samples were stained with Toluidine blue and imaged using a Nikon Eclipse E600FN (Nikon, Tokyo, Japan) with a Nikon D300 DX digital single-lens reflex camera (Nikon, Tokyo, Japan) TEM samples were placed on a copper grid, stained with lead to increase contrast, and imaged using JEOL 1200EX TEM (JEOL Ltd. Tokyo, Japan).

4.6 Demineralization and Deproteinization

Demineralization was done by submersing a spine sample in a solution of 12% hydrochloric acid, 0.07% EDTA, 0.014% sodium tartrate, 0.8% sodium and potassium tartrate, and deionized water, using the protocol as described by Castania, et al. [48].

Deproteinization was achieved by placing the spine in a 2.6% sodium hypochlorite solution for two days. The solution was changed each day. Samples were then rinsed gently with deionized water to get rid of excess sodium hypochlorite solution. After rinsing, samples were dehydrated using hexamethyldisilazane using the protocol described in Appendix E.

4.7 Cantilever Test

Samples were rehydrated with the same method as used for TGA and the spine base was embedded in EpoxiCure 2 resin and hardener (Buehler, Lake Bluff, IL, USA). The samples were left to cure at room temperature overnight. The samples were then sanded down to dimensions to fit in the mechanical testing clamps that are 7.7 mm in thickness, 25.6 mm in width, and 25.4 mm in height. The orientation of the sample is shown in Figure 8. An Instron 3342 (Instron, Massachusetts, USA) instrumented load

frame was used to perform cantilever test with a 500 N load cell. The rate of deflection was 0.003/s.

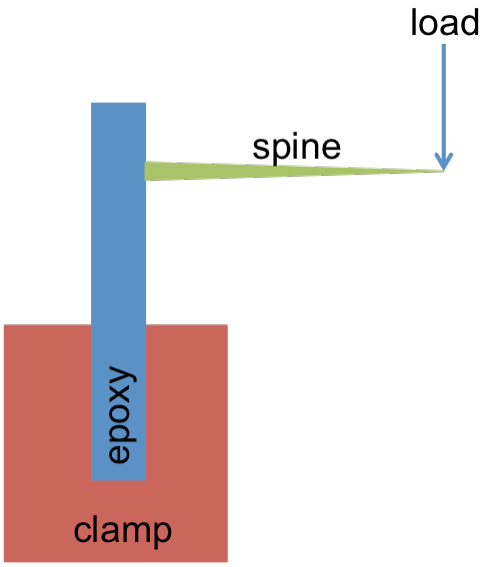

Figure 8. Schematic of spine cantilever test. The clamp is 25.5 mm in width, epoxy is about 3.5 mm in thickness and 8 mm in width. Spines are approximately 5-6 mm in length.

4.7.1 Cantilever Test Data Analysis

Since data was taken for the cantilever test before the deflector was in contact with the sample, the first section of data before the load begins to increase was removed. The deflection at which the load begins to increase was set to 0 to calculate proper tip deflection values. Stress and strain were evaluated using models described in Section 4.7.

4.8 Nanoindentation

Nanoindentation was performed on dried samples of porcupine fish spines using a TI-950 Tribo-Indenter (Hysitron Inc., Minneapolis, MN, USA). Samples were first embedded in epoxy and the surface was polished to a mirror finish using the steps described in the protocol in Appendix G. Nanoindentation maps were made for three

cross-sections: two in section A and one in section C (Figure 20). Only the mineralized regions were tested because dehydration of the collagen-rich areas created an uneven testing surface. A cube corner tip was used to make indentations that were 5 microns apart, with a maximum indentation depth of 300 nm. The displacement function consisted of a 5 second loading step, a 3 second hold, and a 5 second unloading step.

4.8.1 Nanoindentation Data Analysis

Nanoindentation data was analyzed using the Oliver-Pharr method [49], which is described in this section. Parameters measured by the nanoindentation machine are time, depth of indent, and load on the material. In order to find elastic modulus *E* and hardness *H*, the following parameters shown in Figure 9 are used.

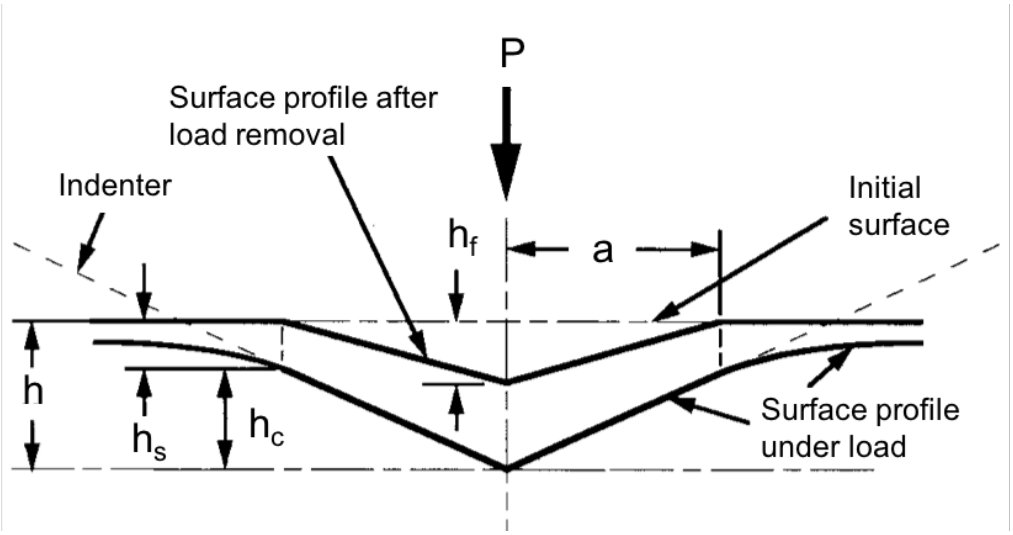

Figure 9. A schematic representation of a material being nanoindented, showing the load *P*, radius of indent *a*, residual hardness impression h_f, contact depth h_c, total displacement of sample *h*, the displacement of the surface of the perimeter of the contact h_s. Figure adapted from Oliver, et al. [49].

The reduced modulus E_r, which accounts for the effects of non-rigid indenters on load-displacement behavior, can be calculated using the following expression:

$$E_r = \frac{\sqrt{\pi}}{2}\frac{S}{\sqrt{A}} \tag{4.2}$$

where S is the slope of the upper portion of the unloading data, A is the projected area of the elastic contact. In the case of a cube-corner tip, the expression for the projected area, which is a function of indenter depth, is

$$A(h_c) = 2.5981{h_c}^2 \tag{4.3}$$

where h_c is contact depth of the experiment. Contact depth for a cube corner tip can be calculated using the maximum load P_{max}, corresponding indenter depth h_{max}, and unloading stiffness S.

$$h_c = h_{max} - \frac{3P_{max}}{4S} \tag{4.4}$$

The reduced modulus is also defined as

$$\frac{1}{E_r} = \frac{1-\nu^2}{E} + \frac{1-{\nu_i}^2}{E_i} \tag{4.5}$$

where E is the elastic modulus of the specimen, ν is the Poisson's ratio for the specimen (taken to be 0.3), and E_i is the elastic modulus for the indenter (1,140 GPa), and ν_i is the Poisson's ratio for the indenter (0.07). Rearranging Equation (4.5), elastic modulus of the specimen can be expressed as the following:

$$E = \frac{1-\nu^2}{\frac{1}{E_r} - \frac{1-{\nu_i}^2}{E_i}} \tag{4.6}$$

Hardness of the sample can be calculated using the expression

$$H = \frac{P_{max}}{A} \tag{4.7}$$

5 Results and Discussion

Images of the *D. holocanthus* and *D. hystrix* are shown in Figure 10. The number of spines on the *D. holocanthus* and *D. hystrix* specimens was approximately 222 and 410, respectively.

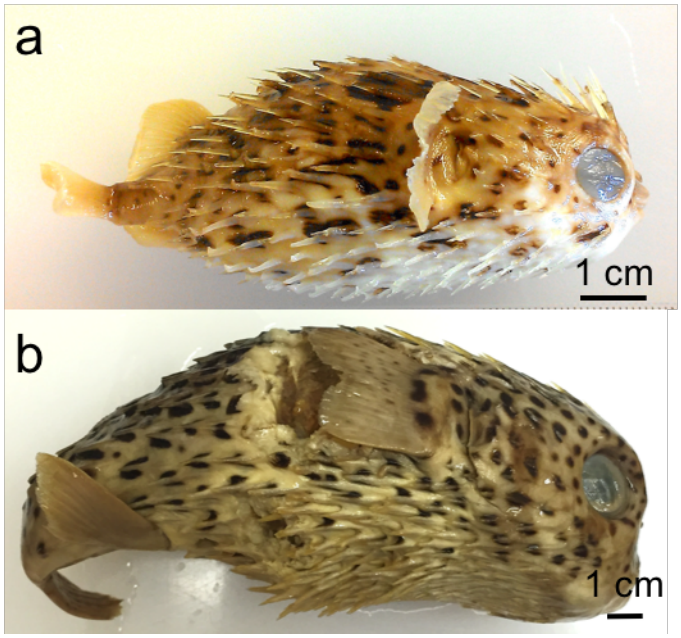

Figure 10. Photographs of the specimens used in this study, **(a)** *Diodon holocanthus* (slender-bodied) and **(b)** *Diodon hystrix* (round-bodied) samples received from the Scripps Institution of Oceanography.

5.1 Material Characterization

5.1.1 Energy-dispersive X-ray Spectroscopy

Energy dispersive X-ray spectroscopy (EDX) was used to identify elements in two regions of the spine: the spinous process and the central part of the spine base. The results of EDX are shown in Figure 11.

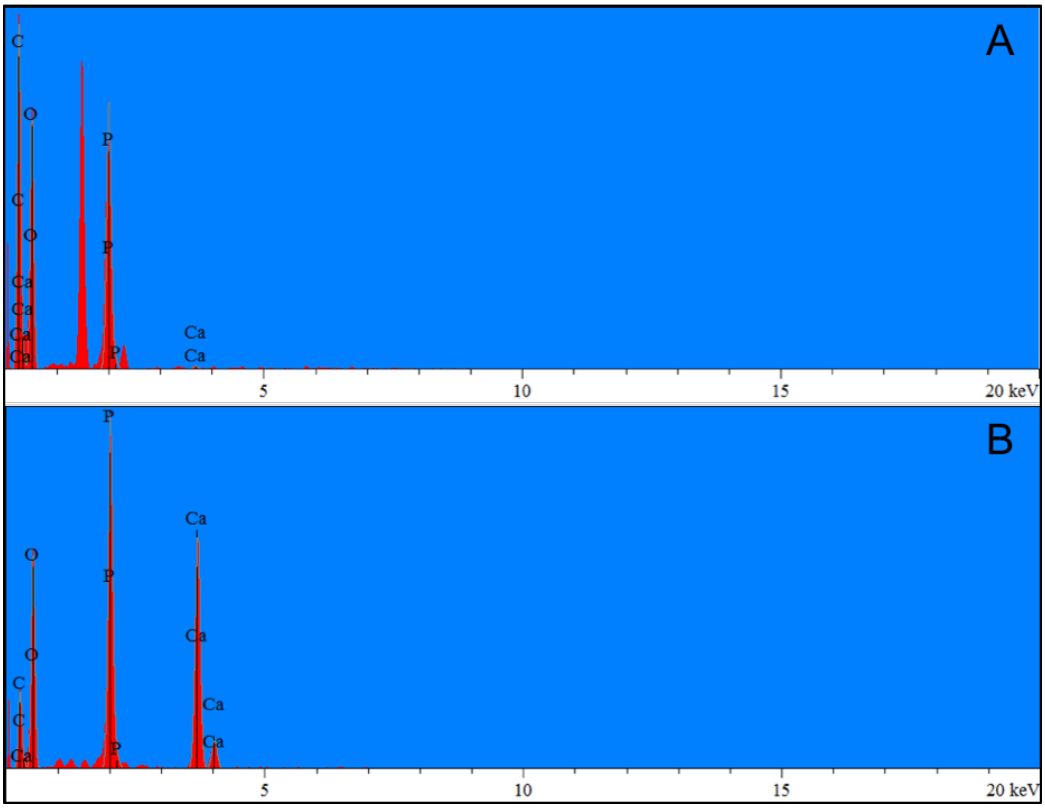

Figure 11. Energy dispersive X-ray spectroscopy spectrums for **(a)** the central region of the spine base and **(b)** the spinous process. In (a) the unlabeled peak is for aluminum left over from the polishing process.

Values in Table 2 were calculated with the Iridium Ultra software (eumeX Instrumentebau GmbH, Heidenrod, Germany) using the ZAF algorithm, which calculates the mass and atomic percentages using the area under the spectroscopy curves, atomic number, absorbance and fluorescence of the sample. From the high carbon content and extremely low calcium content, it is reasonable to assume that the center of the spine base is mostly, if not completely, composed of organic material. However, it is unclear why there are high concentrations of phosphorus, which is generally not present in collagen amino acids. The composition of the spinous process implies that it has a mixture of organic and mineral material. The organic component of the porcupine fish spines is most

likely collagen, which is found in many other fish spines, as mentioned in Section 2.2.3. Given the high atomic percentage of phosphorus in the region with high concentrations of calcium, the porcupine fish spine most likely contains hydroxyapatite ($Ca_{10}(PO_4)_6(OH)_2$).

Table 2. Comparison of elemental composition between spine base center and spinous process.

Element	(A) Spine Base Center (atomic %)	(B) Spinous Process (atomic %)
C	57.85	16.32
O	29.74	40.08
P	12.06	19.68
Ca	0.35	23.91

5.1.2 X-ray Diffraction

XRD was used to confirm the presence of hydroxyapatite in the porcupine fish spine. As seen in Figure 12, the peaks of each region of the spine match the standard XRD pattern for hydroxyapatite (PDF 01-076-0694). The broad peaks in the pattern indicate that the sample is nanocrystalline. Crystallite sizes were calculated using Scherrer's equation (Equation (4. 1)) using peaks (221), (-380), and (242). The average values for the crystallite sizes are ~20.1 nm, ~20.4 nm, and ~20.8 nm for the spinous process, lateral processes, and spine base, respectively. These crystallite sizes are similar to that of bovine femur bone [50]. It is of note that while other fish scales have been known to contain calcite as mentioned in Section 2.2.3, no calcite was found in the porcupine fish spines.

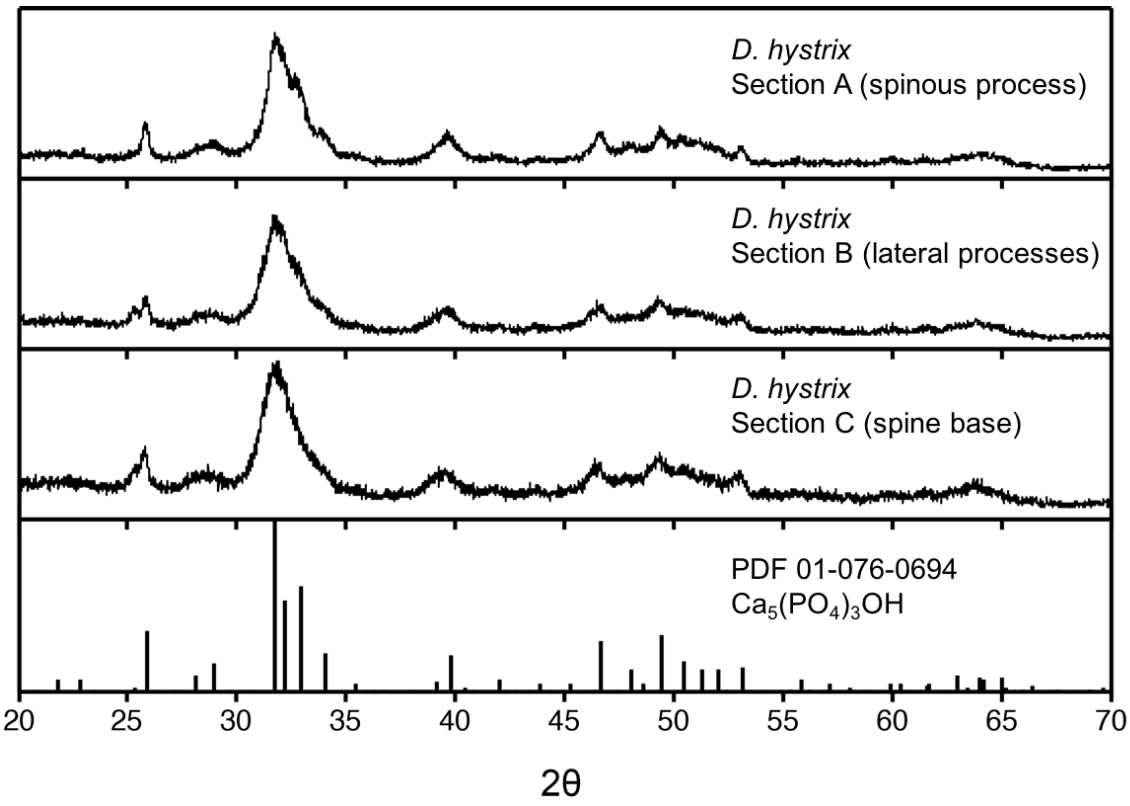

Figure 12. X-ray diffraction pattern of different sections of the *D. hystrix* spine. From top to bottom: XRD pattern for sections A, B, and C of the spine and the standard XRD pattern for monoclinic hydroxyapatite.

5.2 Micro-Computed Tomography & Nano-Computed Tomography

μ- CT was performed on a *D. holocanthus* specimen and show mineralized spines. In addition, spines create a layer of subdermal armor as a result of lateral processes that extend beneath each other (Figure 13). The mouth of the porcupine fish is also highly mineralized (Figure 13b).

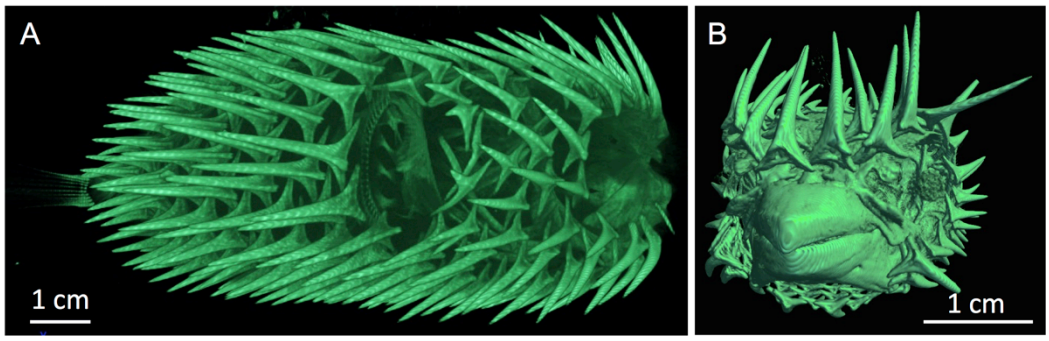

Figure 13. Micro-computed tomography of porcupine fish *D. holocanthus* showing **(a)** lateral and **(b)** anterior view. Voxel size of 12.56 µm was used.

Nano-CT (Figure 14) shows that each spine is composed of three distinct parts and corroborates previous results [28]. As described in Section 2.2.3 and shown in Figure 6, the axial process is significantly shorter than the lateral processes, which allows the spine to be erected during inflation. The spine seems to start from the axial and lateral processes and slowly combine into the spinous process. It can also be that the spine tip is much denser than the rest of the spine. However, there appears to be a layer of less dense material surrounding the dense spine mineral.

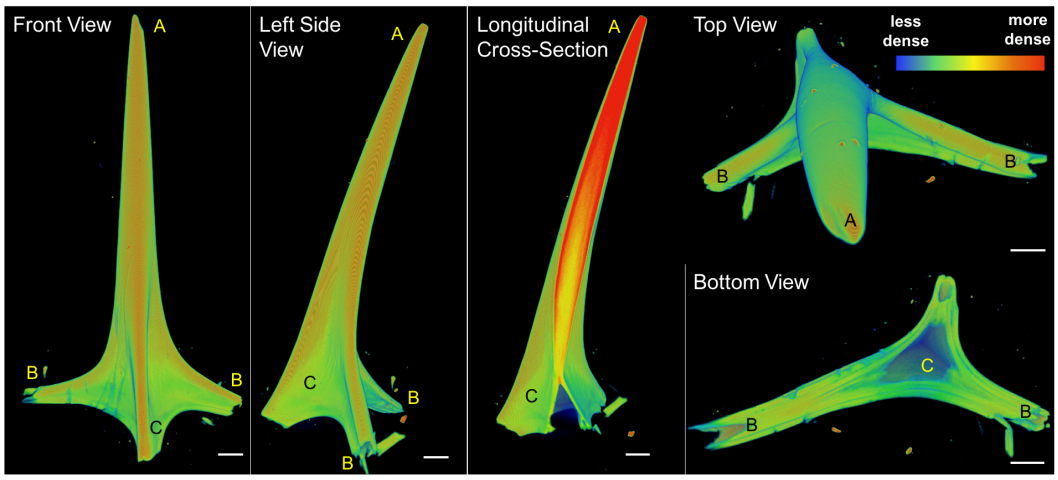

Figure 14. Nano-computed tomography of porcupine fish spine. Each scale bar is 500 µm. Spine coloration represents density of the sample. Red symbolizes regions of highest density and blue represents regions of lowest density. The front view and left side view of the spines show different sections A, B, and C of the spine.

5.3 Thermogravimetric Analysis

Thermogravimetric analysis revealed that each section of the spine has a different composition of mineral, protein and water. Figure 13 shows three representative TGA curves for the spinous process, the lateral processes, and the spine base, which includes the axial process. Mass loss between room temperature and 250˚C corresponds to water loss [47, 51], and during mass loss from 250˚C to 700˚C protein decomposition and combustion occurs [47]. Compositions of sections A, B, and C are summarized in Table 3, where values are given as mean ± standard deviation. Variations in protein and water content are attributed to limitations of sample preparation. Excess tissue was difficult to completely remove from sections B and C. Section C has the largest amount of protein and water, while section A has the most mineral. This confirms the results from the nano-CT, since the denser regions in the nano-CT correspond to the more mineralized section A. The weight percentage of mineral in section A is similar to that of bovine femur (67 wt%) [23].

Table 3. Average water, protein, and mineral (wt.%) in *D. holocanthus* spine. Values are given as average ± standard deviation.

	A	B	C
Water	18 ± 1.2	36 ± 15.2	59 ± 6.2
Protein	19 ± 0.6	25 ± 4.2	23 ± 2.7
Mineral	63 ± 1.4	39 ± 15.0	17 ± 7.2

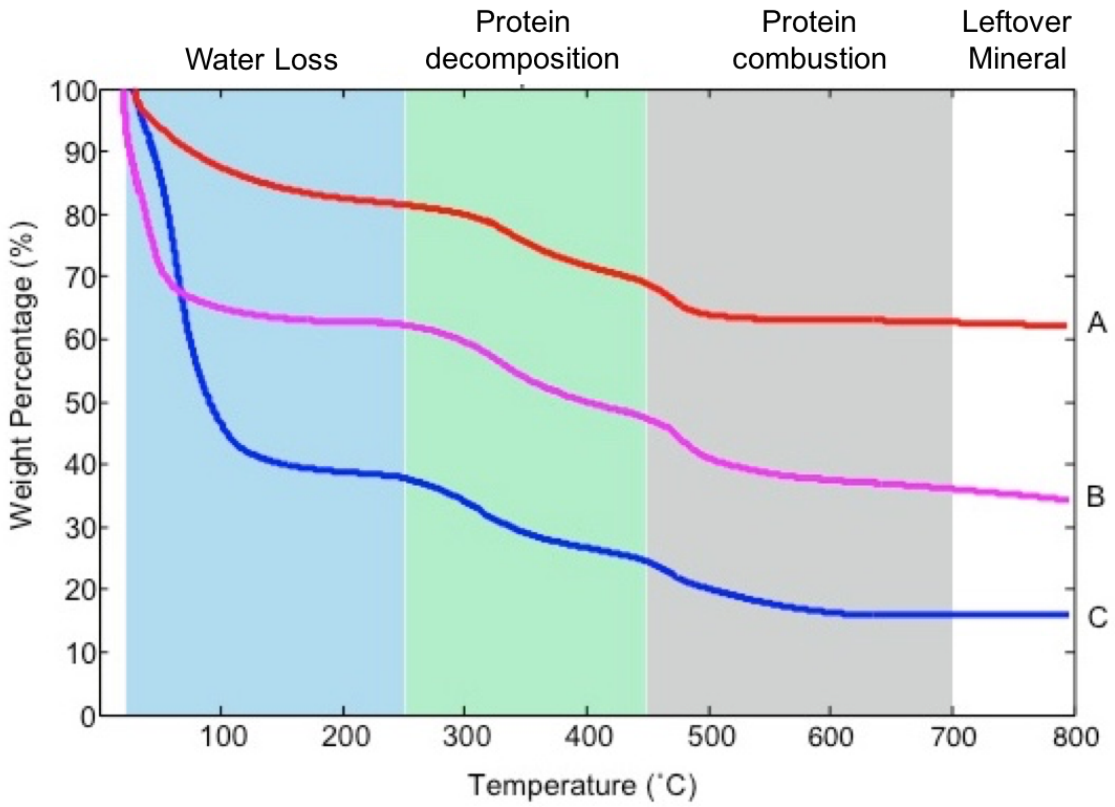

Figure 15. Representative thermogravimetric curves for different sections of porcupine fish spine A, B, and C. Water loss occurs between room temperature to approximately 250˚C. Protein decomposition and combustion occurs from 250˚C to 700˚C. The remaining mass after the sample has reached about 700˚C is mineral.

5.4 Light Microscopy

A concentric ring pattern can be seen in the transverse cross-section of the spine (Figure 16 inset) and is represented in Figure 16. These growth rings have widths that range from 2 to 3.5 μm per ring. Growth rings are commonly seen in many other fish scales and have been often used to distinguish the age of a fish by correlating mass increase per year with width of growth rings [52]. However, no work has been done to determine the age of porcupine fish using the growth rings in the spine.

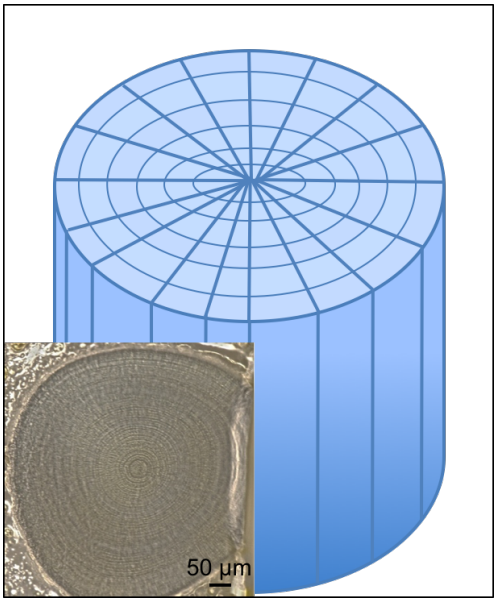

Figure 16. Representation of *D. hystrix* spine transverse cross-section showing concentric ring structure. (Inset) Light microscopy image of spine cross-section that was embedded in epoxy and polished.

After staining thin sections with toluidine blue, a radial pattern was observed (Figure 17). Toluidine blue stains acidic components such as nucleic acids and proteins, meaning that the dark lines are more mineralized than the blue-stained areas. Radiating mineral columns have been observed in a variety of fish scales including elasmoid scales of the goldfish [53]. The radial and concentric structures observed in the spine cross-sections may benefit the spines mechanically by deflecting cracks and strengthening the spine during bending.

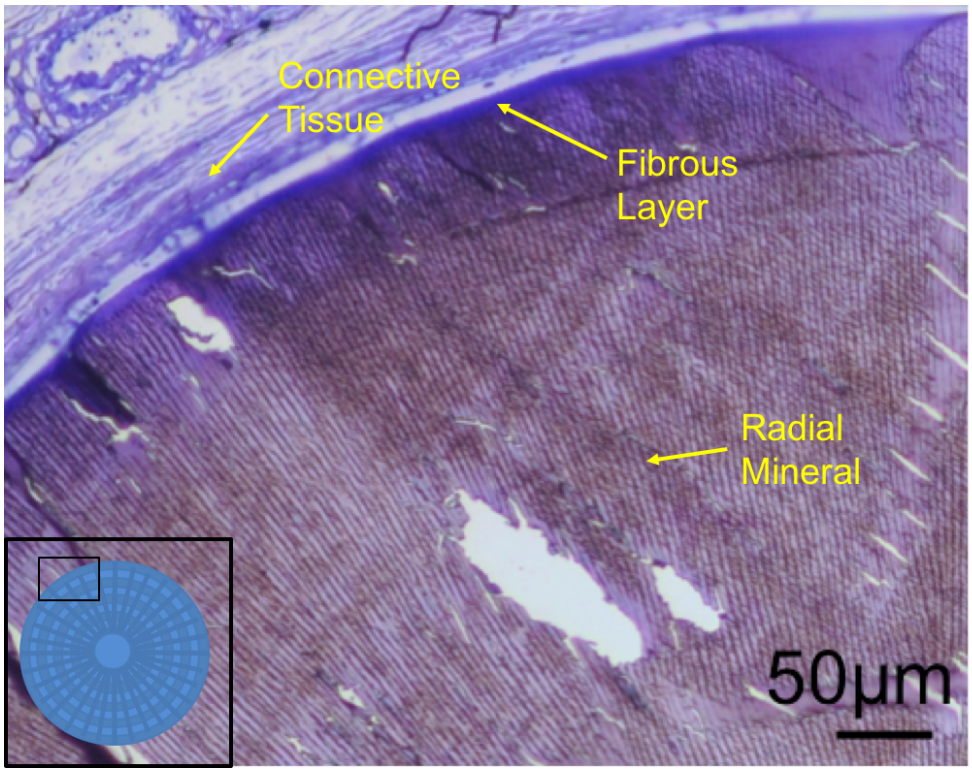

Figure 17. Light microscope image of toluidine blue stained transverse cross-section of *D. hystrix* spine in section A (shown in Figure 4). A radially aligned pattern of mineral can be observed. Inset image shows the portion of the transverse cross-section that main image is taken from.

5.5 Scanning Electron Microscopy

5.5.1 Macrostructure and Layers

Figure 16a shows a freeze-fractured *D. hystrix* spine surface, where the tip of the spine is pointing to the right. Figure 16b shows the layered structure of the porcupine fish spine. Figure 16c shows the outer connective tissue, which attaches the spine to the outermost layer of skin. From XRD, it is known that there is hydroxyapatite in the sample and from EDX done on the spine longitudinal cross-section (Section 5.1.1), there is high calcium and phosphorous content, which indicates that the core is mineralized (Figure 18d). This core also shows the step-like fracture surface, which implies a layered internal

structure. Finally, a porous and fibrous layer sandwiched between the mineral core and connective tissue is shown in Figure 18e. This porous and fibrous layer was stained a deep blue in histology results (Section 5.4), which could imply the presence of cells and that the growth front of the spine is at the interface between the mineralized core and the fibrous layer. Overall, the structure is layered as shown in Figure 18f.

The transverse cross-section of a deproteinized spinous process is shown in Figure 19. The empty center implies that the spinous process may not be completely mineralized near the center. This would explain the results from nano-CT cross-section shown in Figure 14 (Section 5.2), which shows a yellow-orange color in the middle of the spine. This implies a less dense spine core, but one that is denser than the protein packed base, which is colored blue in the micro-CT.

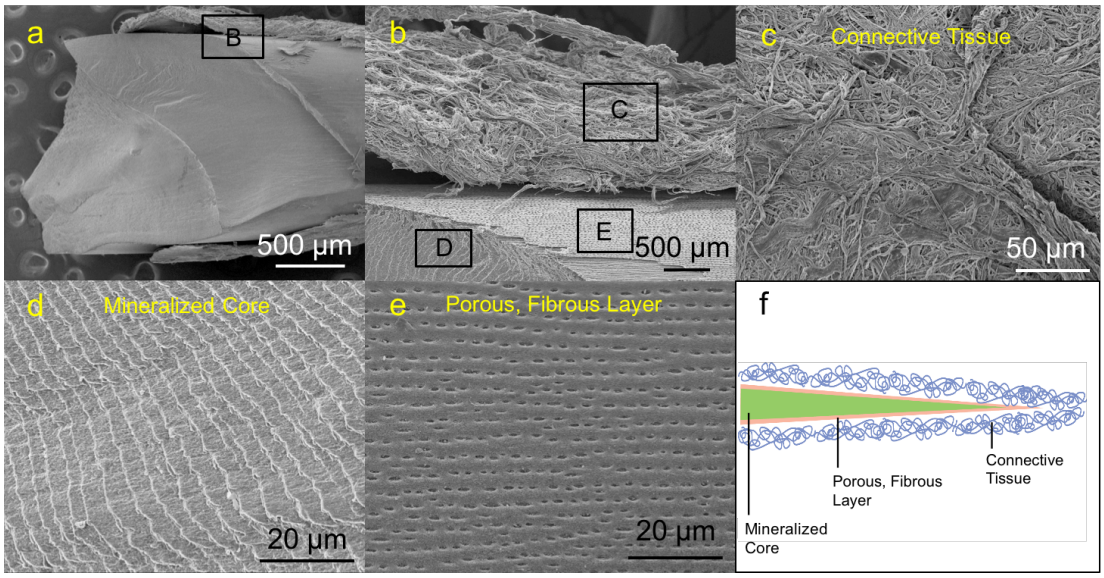

Figure 18. Scanning electron micrograph of freeze-fractured *D. hystrix* spine layered structure. **(a)** shows the freeze-fractured surface of the spine where the tip is pointing to the right. **(b)** is the boxed area B in (a) that shows the combination of layers that make up the spine. Boxed areas in (b) correspond to images shown in (c), (d) and (e). **(c)** is connective tissue **(d)** is the mineralized core, and **(e)** is the porous fiber layer. **(f)** is an overall schematic of the layers in the spine.

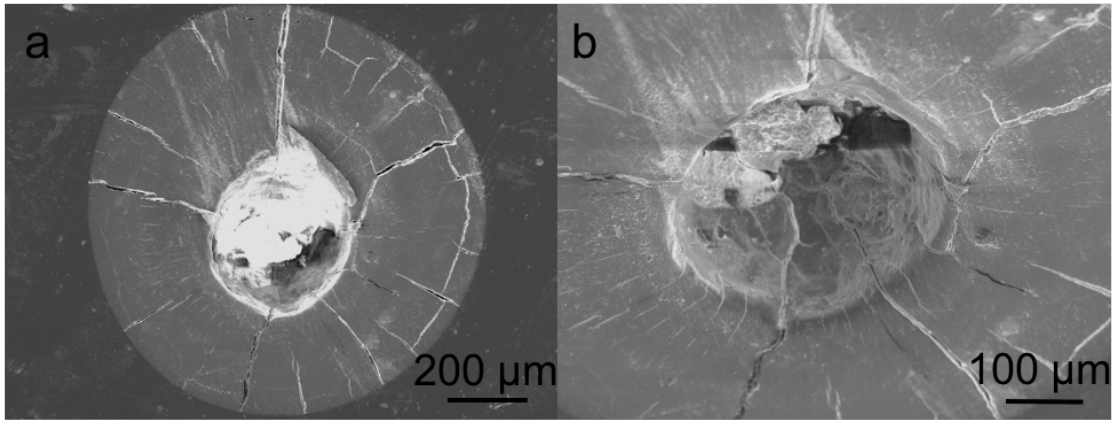

Figure 19. Transverse cross-section of deproteinized spinous process. **(a)** shows radial cracks and an empty spine center. **(b)** shows the cross-section imaged at a 45˚ angle to show the empty space in the center of the spine.

5.5.2 Microstructure Observed through Cross-Sections

Fibers from the base of the spine have banding that appear to match that of collagen (Figure 20), however calculated values of the d-spacing of approximately 60 nm, whereas the d-spacing of collagen should be 67 nm. This mismatch may be a result of improperly calibrated working distance when capturing the image or fibers being tilted from the beam.

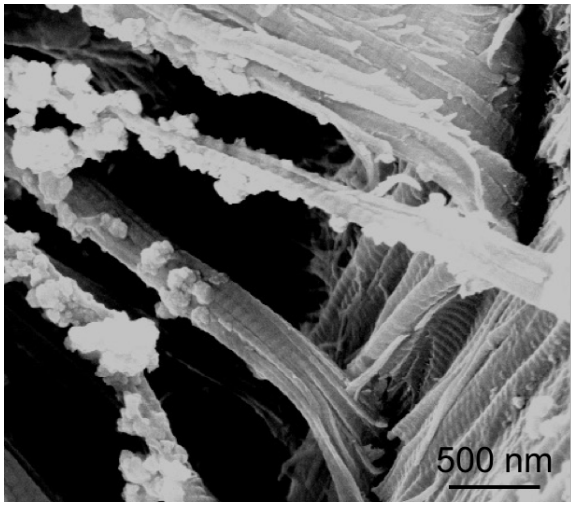

Figure 20. Scanning electron microscopy image of banded fibers located in the spine base. The banded structure is indicative of collagen.

From the histology results in Section 5.4, it is known that there is radial symmetry and patterning in the transverse cross-section of the spine. This is corroborated and clearly seen in the untreated and demineralized spine SEM images in Figure 21.

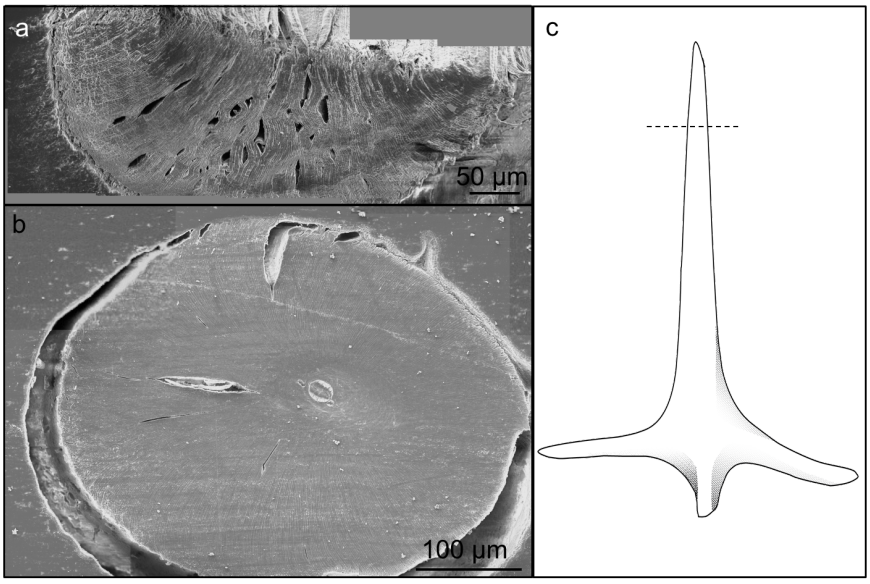

Figure 21. Transverse cross-sections of **(a)** the deproteinized spine and **(b)** untreated spine showing radial material alignment. **(c)** is a schematic of the spine, with the dotted line indicating where the spines were cut.

The polished longitudinal cross section of the tip of the porcupine fish spine shows that mineralized fibers are aligned longitudinally (Figure 22). Observing that there are both longitudinally aligned fibers and radially symmetric material in the transverse axis, it can be concluded that the longitudinal fibers form sheets of fibers with widths of 1.7 ± 0.3 µm that are aligned radially. Sheets of mineralized collagen fibers have been observed in other fish scales as well [53]. Figure 23 shows that the longitudinally aligned fibers are connected by mineral bridges. The mineral bridges are reminiscent of those in nacre, which are believed to prevent crack propagation and sliding between aragonite plates [54, 55]. The mineral bridges in the porcupine fish spine may serve a similar purpose, by preventing the fibers from sliding.

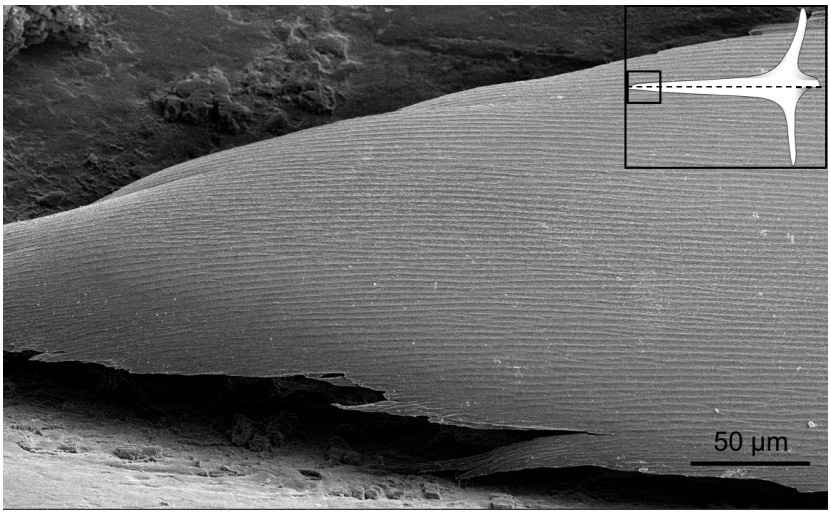

Figure 22. Longitudinal cross-section of *D. holocanthus* spine showing aligned mineralized fibers. Inset diagram shows where spine was cut (along dotted line) and location on spine that image was taken (boxed area).

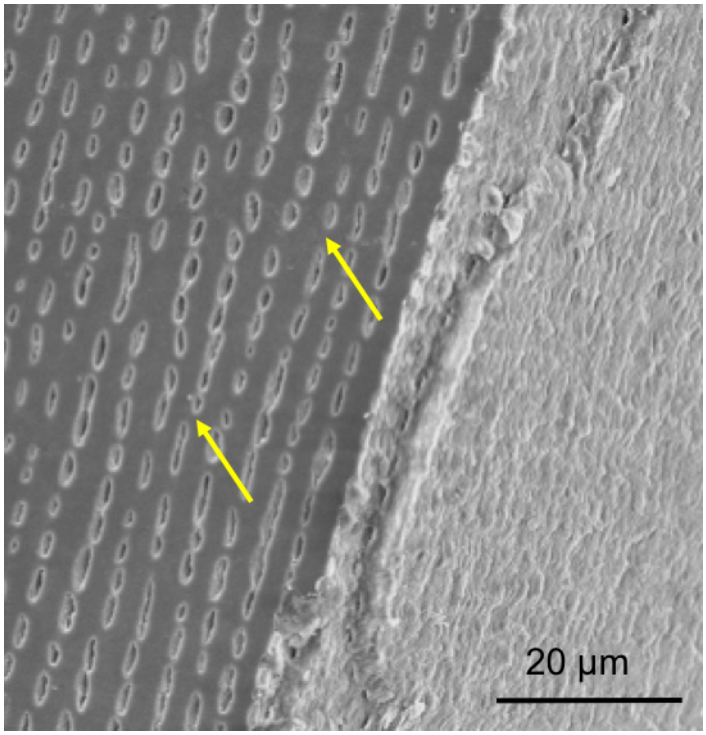

Figure 23. Polished, longitudinal cross-section of deproteinized spine showing mineral bridges between fiber sheets.

The growth rings in the porcupine fish spine can also be seen using SEM (Figure 24). The widths of the rings matched those found in optical microscopy described in

Section 5.4. The combination of the concentric rings and radial sheets may contribute to increasing the toughness of the spine through crack deflection, which is observed in Figure 25.

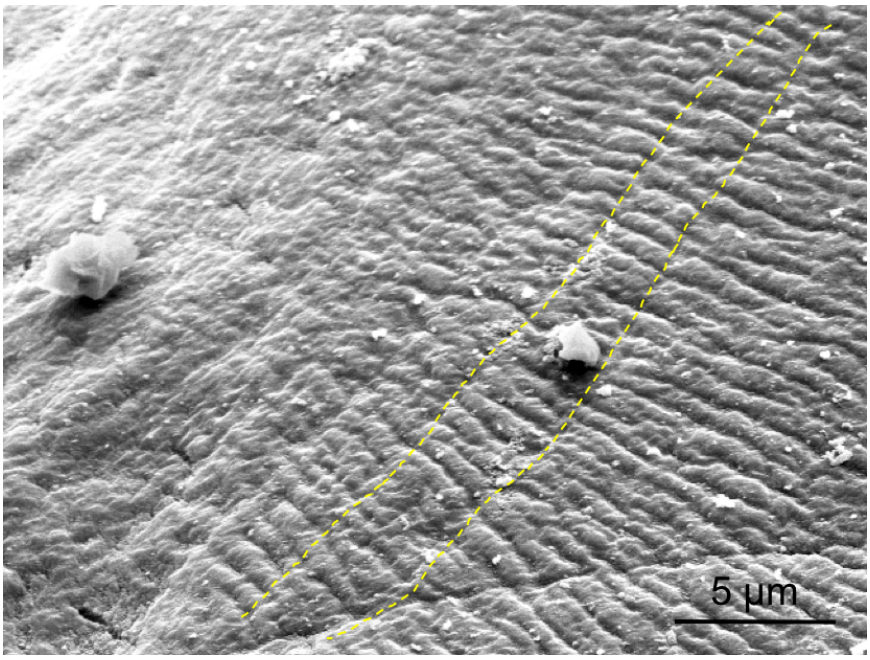

Figure 24. Scanning electron microscopy image of concentric ring structure. The width of one ring is outlined in dotted yellow lines.

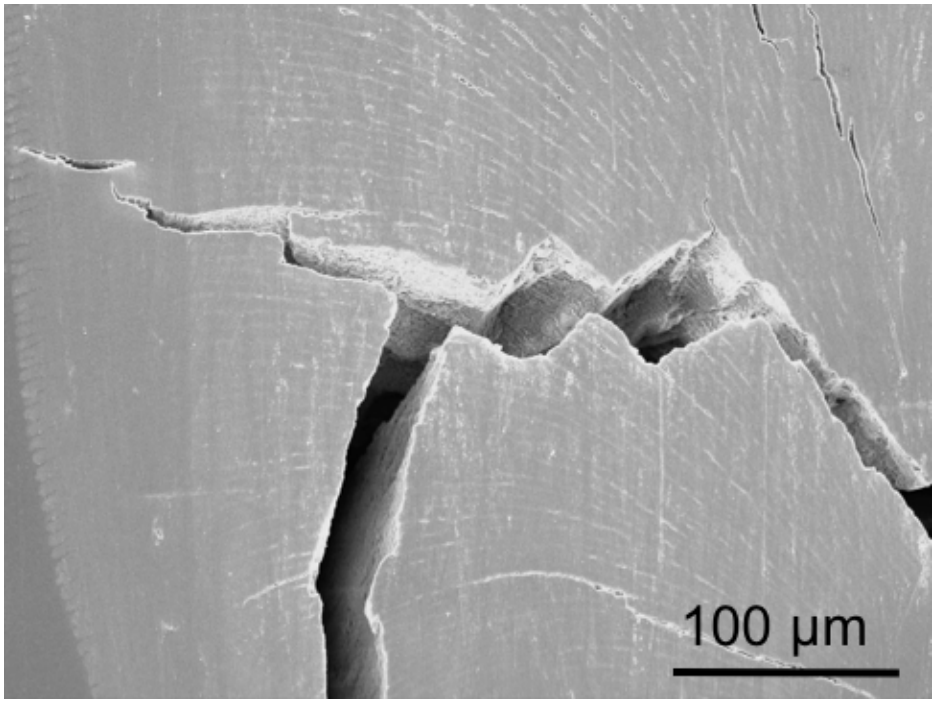

Figure 25. Cross-section of *D. hystrix* spine, showing crack deflection through the spine.

5.6 Transmission Electron Microscopy

Spine thin sections of the transverse cross-section stained with osmium tetroxide and lead confirmed the presence of radially aligned mineral structures inside the porcupine fish spine. The mineral is embedded within a fibrous matrix and forms sheets with widths of about 2 µm (Figure 26). Measurements from SEM show that the demineralized spine radial sheets seen in Figure 21a are approximately 1.7 µm. The slightly larger width of the TEM imaged sheets are a result of the presence of hydroxyapatite nanocrystals that extend beyond the fiber.

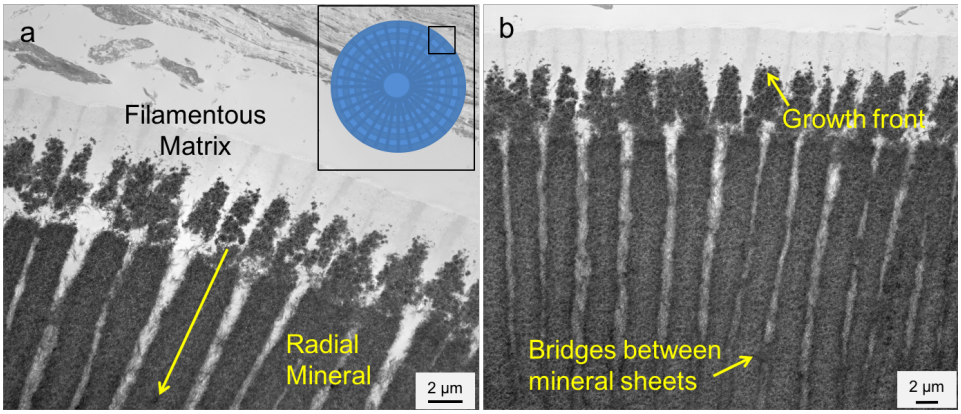

Figure 26. Transmission electron micrograph of spine transverse cross-section. Dark columns are mineral embedded a fibrous matrix. Arrow points toward the center of the cross-section.

Putting together all of the microstructural information, it can be seen that the spine has the structure described in Figure 27. In the longitudinal direction, mineralized fibers are connected by mineral bridges to form sheets that align radially. In between these sheets, there are fibers that are aligned in the transverse direction.

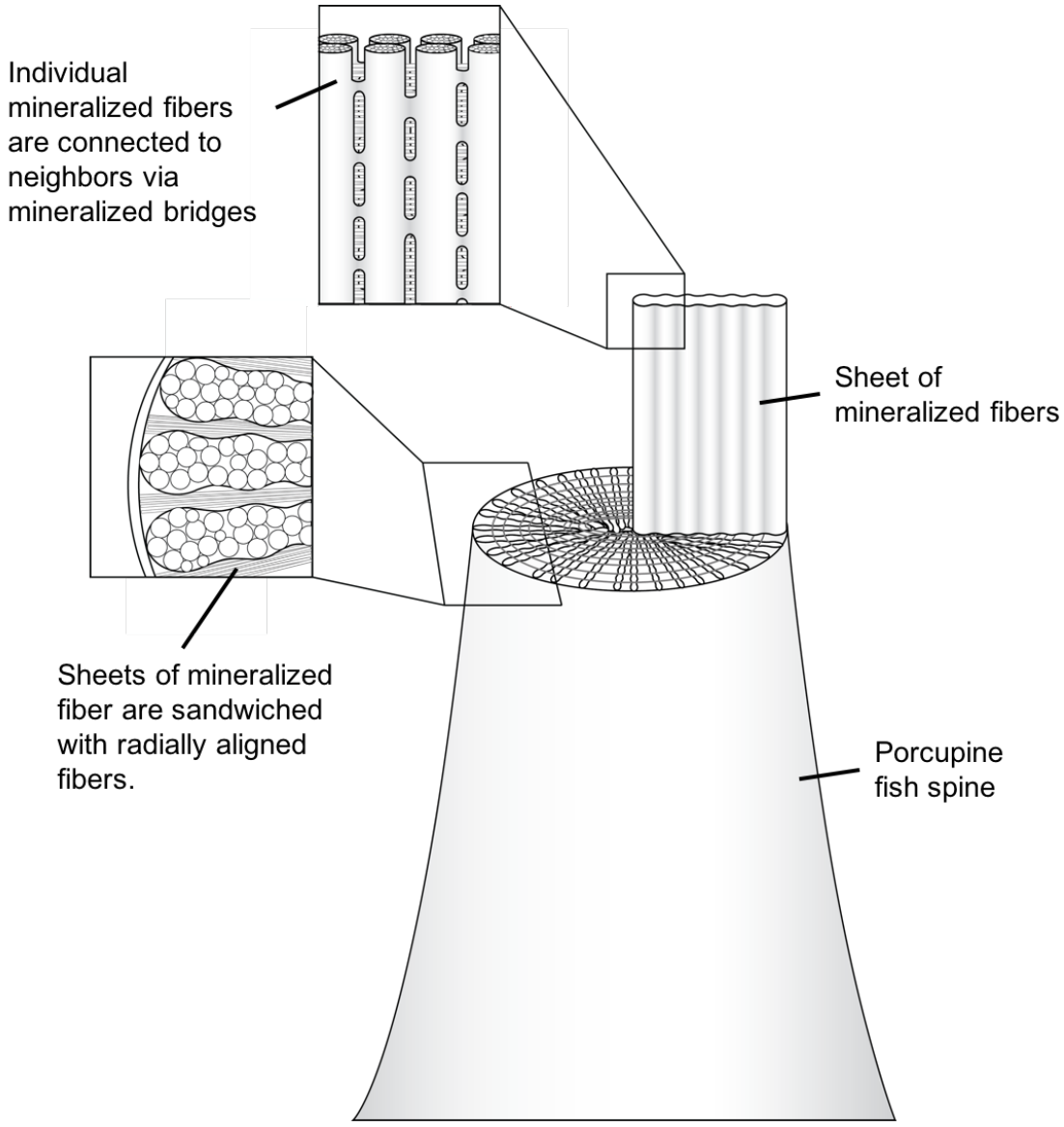

Figure 27. Schematic diagram of the hierarchical structure of a showing orientation of mineralized sheets and radially aligned fibers.

5.7 Nanoindentation

Nanoindentation was performed on three transverse cross-sections of the *D. holocanthus* spine (shown in Figure 28 and Figure 29). Two cross-sections were taken in section A near the spine tip, and one cross section was taken in section C. Young's modulus and hardness values were calculated using the values from the force-

displacement curves of each indent (representative force-displacement curve shown in Figure 30) and the equations described in Section 4.8.1. As a result of the symmetric nature of the spine cross-sections, partial nanoindentation maps were made across transverse cross-sections of the spine. Points with extremely low modulus and hardness represent an indentation in the epoxy surrounding the sample and were removed. Since no distinct patterns or abrupt changes in modulus and hardness were found across the tested area, the remaining values from nanoindentation were averaged across each cross-section.

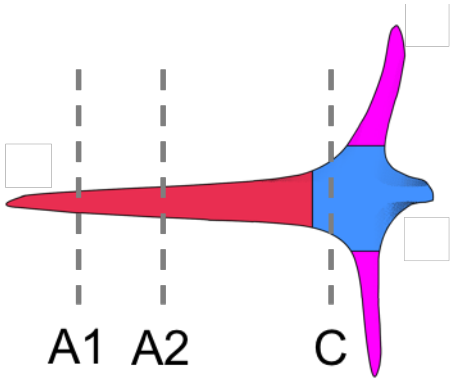

Figure 28. Schematic of cross-sections that were tested using nanoindentation.

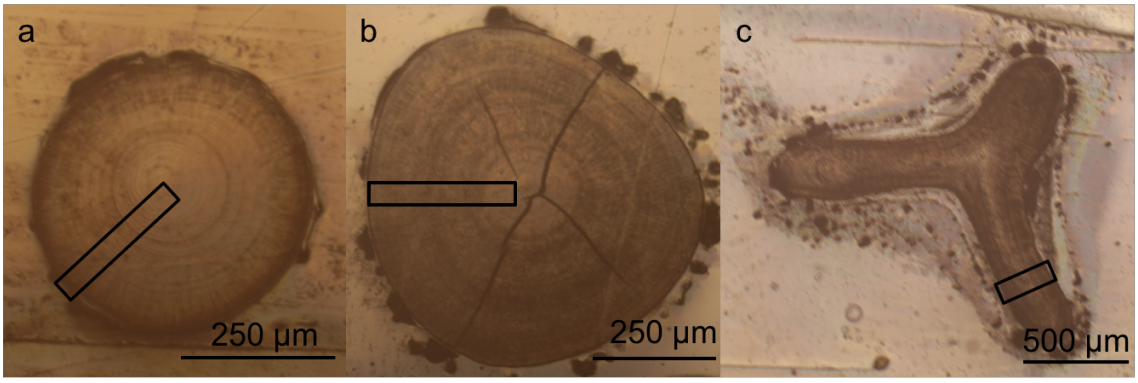

Figure 29. Locations nanoindented for **(a)** section A1, **(b)** section A2, and **(c)** Section C. The cracks in (b) are due to dehydration.

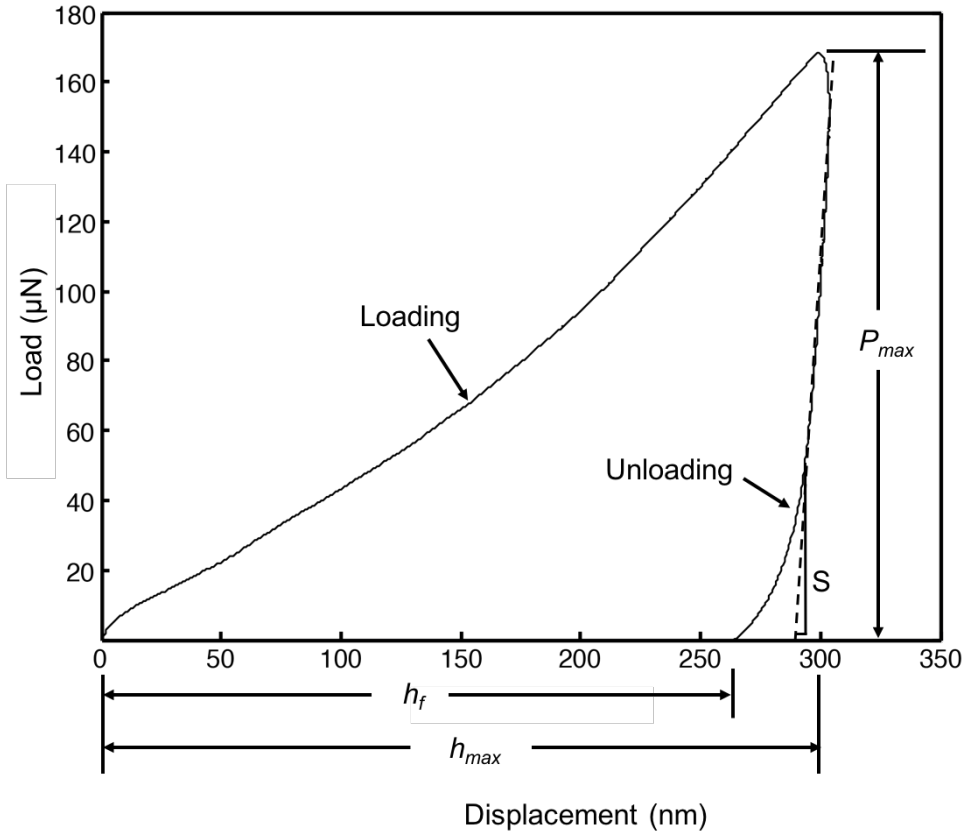

Figure 30. Representative load-displacement curve for nanoindentation on a transverse sample from a *D. holocanthus* spine. *S* is shown as the initial slope of the unloading curve. *Pmax* is the maximum load and h_{max} is the displacement at *Pmax*. h_f is the residual hardness impression.

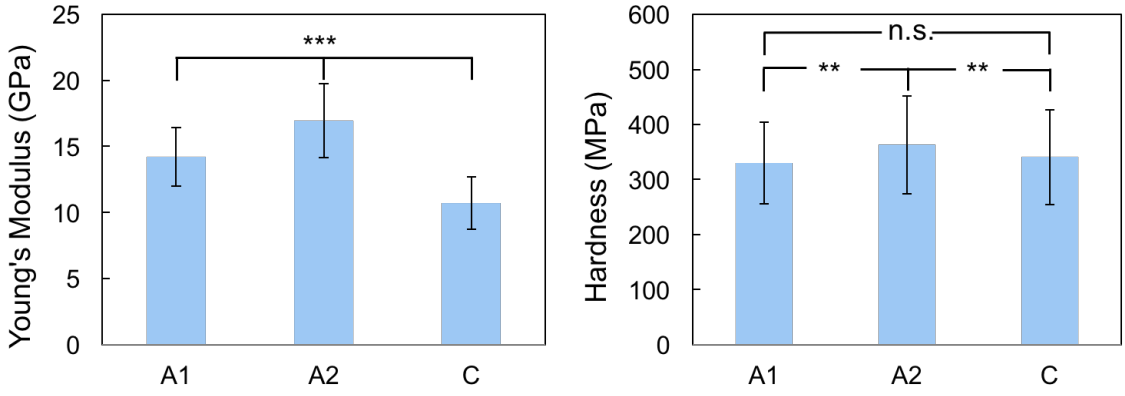

Figure 31. Average Young's modulus and hardness values from nanoindentation of sections A1, A2, and C. *, **, and *** represent p≤0.05, 0.01, and 0.001, respectively using a two-tailed t-test. n.s. represents p values greater than 0.05, for which the difference between two sets of data is not significant.

Table 4. Number of indents for samples A1, A2, and C.

	A1	A2	C
Number of Indents	76	296	200

Results of nanoindentation are shown in Figure 31 with number of indents per sample listed in Table 4. The large standard deviations are typical of biological materials. A two-tailed t-test was used to determine whether values are significantly different. Young's modulus values across the different sections were found to be significantly different. The Young's modulus of section A2 was higher than both A1 and C even though the A2 cross-section is located between the two other points. The lower stiffness in section C is reasonable since the base of the spine is less dense and mineralized than the sections on the spinous process. Hardness values of A1 and C were found to be significantly different from the hardness of section A2. However the hardness of section A1 was not significantly different from the hardness of section C. Nanoindentation results imply that the area near the tip of the spine is more mineralized, which matches what was found in the nano-CT results.

5.8 Modeling Mechanical Behavior and Mechanical Tests

Using basic mechanical engineering equations, mechanical models were developed and used to calculate, maximum tensile strength, maximum strain, elastic modulus, and elastic energy for spines tested using a cantilever test. Two models of the porcupine fish spine are compared: the spine as a uniform cylindrical beam and the spine as a tapered beam with a circular cross-section (both shown in Figure 32). P is a point load at the end of the cantilever beam, d is the diameter of the cylindrical beam, and L is the length of the

beam. In order to better represent the shape of the porcupine fish spine, the spine is represented as a tapered beam as shown in Figure 32. Equations for the two models are derived in Appendix A and Appendix B and summarized in Table 5.

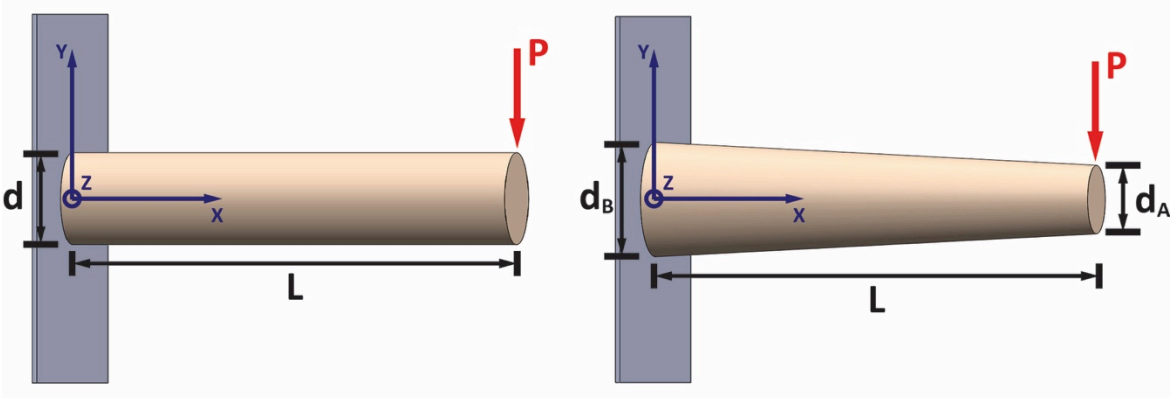

Figure 32. (Left) Uniform cylindrical cantilever beam with a constant diameter *d*. **(Right)** Tapered cylindrical cantilever beam where d_B is the larger diameter of the beam, d_A is the smaller diameter of the beam. *L* is beam length and *P* is the point load at the end of the beam for both models.

Table 5. Equations of mechanical properties for uniform cylinder and tapered cylindrical beam models. For the *D. holocanthus* spines, $\beta \sim 0.2$.

	Uniform Cylindrical Beam	Tapered Beam
Maximum Tensile Stress	$\sigma_{max} = \frac{32\ PL}{\pi\ d^3}$	$\sigma_{max} = \frac{128PL}{27\pi {d_B}^3 \beta^2(1-\beta)}$
Elastic Modulus	$E = \frac{64\ P\ L^3}{3\pi v_{max}\ d^4}$	$E = \frac{64\ P\ L^3}{3\pi\beta {d_B}^4 v_{max}}$
Strain at Maximum Stress	$\varepsilon_{max} = \frac{3v_{max}d}{2L^2}$	$\varepsilon_{max} = \frac{2v_{max}d_B}{9\beta(1-\beta)L^2}$

Using the equations for maximum tensile stress listed in Table 5, the maximum tensile stress at the top surface of the spine σ_{max} was plotted with distance away from the fixed end *x* (Figure 33). *P*, *L*, d_B, and β values used to create the plot are averages of values found from tested specimens. The diameter *d* of the uniform cross-section beam was calculated by equating the volumes of the two types of beams. The volume for the tapered beam $V_{tapered}$ is the same as that of a truncated cone

$$V_{truncated\ cone} = \frac{\pi h}{3}(r^2 + rR + R^2) \tag{5.1}$$

where *h* is the height of the truncated cone, *r* is the radius of the small circular area, and *R* is the radius of the large circular area. Inputting the parameters for the spine, it follows that

$$V_{tapered} = V_{truncated\ cone} = \frac{\pi L}{3}\left(\frac{{d_A}^2}{4} + \frac{d_A d_B}{4} + \frac{{d_B}^2}{4}\right) = \frac{\pi L}{12}\left({d_A}^2 + d_A d_B + {d_B}^2\right)$$

$$V_{tapered} = \frac{\pi L}{12}\left({d_A}^2 + d_A d_B + {d_B}^2\right) \tag{5.2}$$

The volume of the uniform cross-section beam $V_{uniform}$ is

$$V_{uniform} = \pi\left(\frac{d}{2}\right)^2 L \tag{5.3}$$

Setting Equation (5.2) equal to Equation (5.3),

$$\pi\left(\frac{d}{2}\right)^2 L = \frac{\pi L}{12}\left({d_A}^2 + d_A d_B + {d_B}^2\right) \tag{5.4}$$

Rearranging the equation yields the following expression

$$\frac{d^2}{4} = \frac{1}{12}\left({d_A}^2 + d_A d_B + {d_B}^2\right)$$

$$d = \pm\sqrt{\frac{{d_A}^2 + d_A d_B + {d_B}^2}{3}} \tag{5.5}$$

where the value of d must be positive.

From Figure 33 it can be seen that the maximum stress in the tapered beam is slightly higher than that of the uniform beam. However, the location at which the maximum stress occurs changes from the fixed end of the beam for a uniform cross-section beam to a distance close to the tip of the beam for a tapered beam. This may be beneficial so that if the spine in the porcupine fish does break, it breaks near the tip, and most of the spine material will be conserved. It is also important to note that the results from nanoindentation show that the area near the tip is stiffer and harder, which may indicate that the spine is reinforced where the stress is largest.

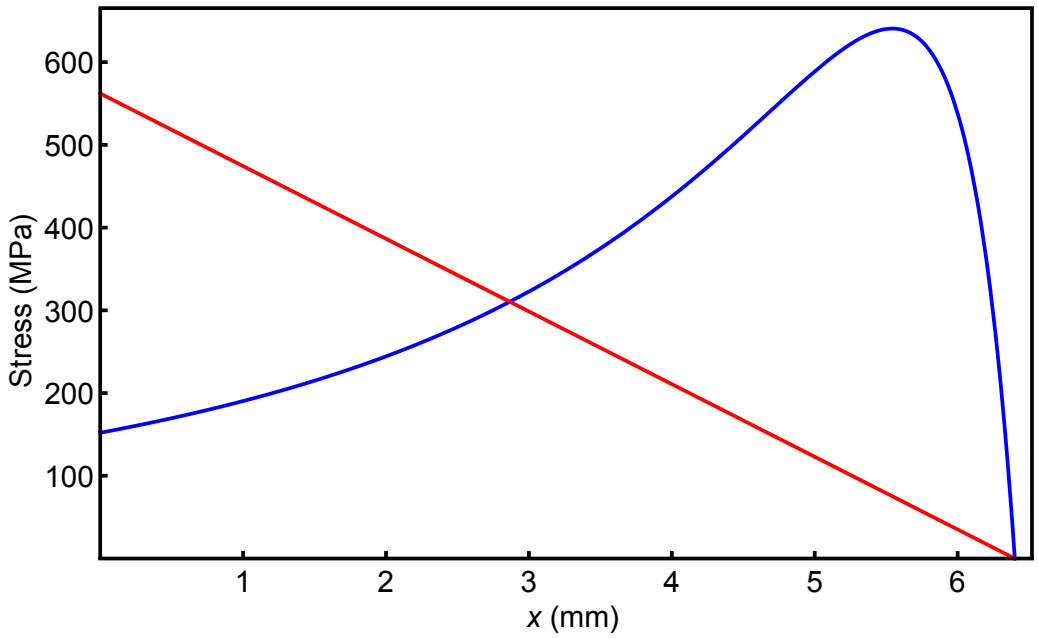

Figure 33. Stress at top of beam as a function of x from 0 to the length of the beam L, where the red curve represents the stress in a uniform cylindrical beam and the blue curve represents the stress in a tapered beam with circular cross-section. Values used for P, L, d_B, and β are averages from experiments. Volumes of the two beams are equal.

After testing five *D. holocanthus* spine samples, the equations for the two different models were applied to the data (representative load-displacement curve shown in Figure 34. Diameter of the uniform beam d was calculated using Equation (5.5) so that volumes were kept constant between models. It can be observed from Table 6 that for an average tapering ratio β of approximately 0.2, the average maximum tensile stress increases for a tapered beam, Young's modulus decreases, and strain at failure increases when compared to that of the uniform beam. The Young's modulus of the tapered beam model also corresponds well with values found in nanoindentation ($E \approx 11 \sim 17$ GPa). Values from nanoindentation are likely higher than those calculated from mechanical tests, since the nanoindented samples were dried and cantilever test samples were hydrated. It is well known that dehydrated samples have higher stiffness [56].

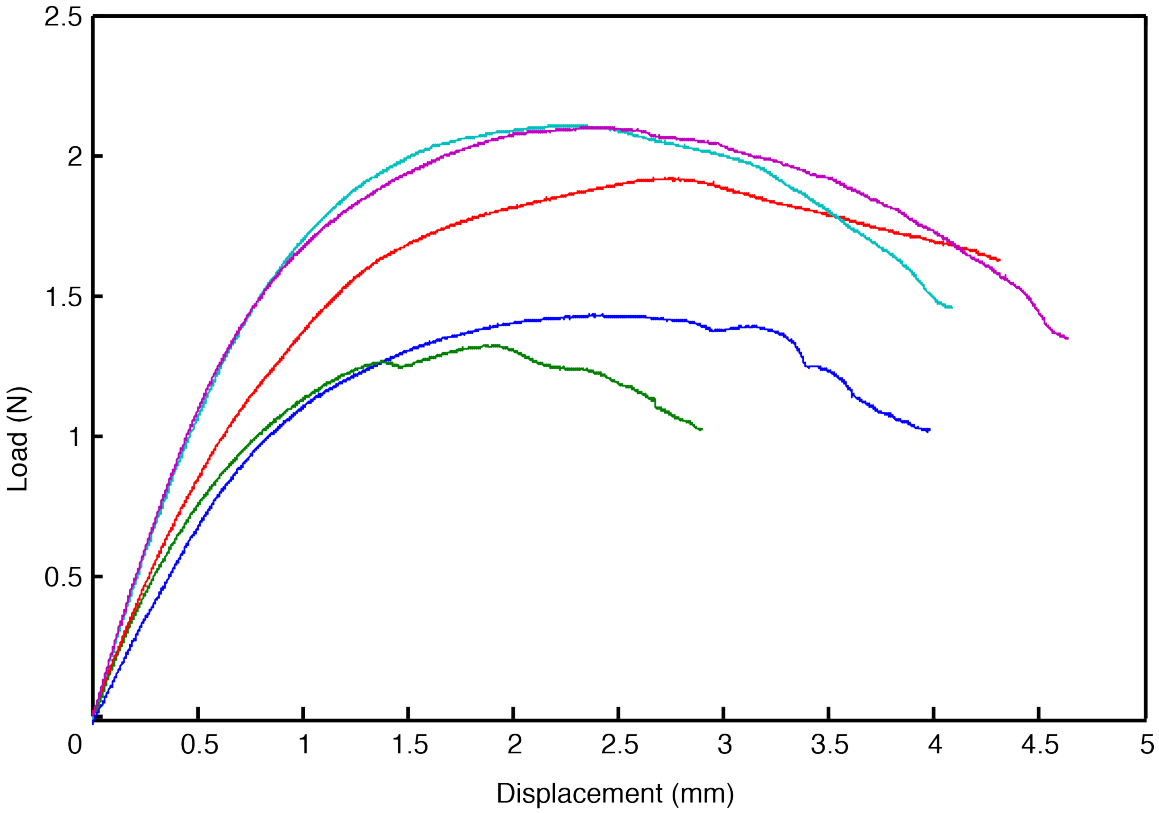

Figure 34. Representative load-displacement curve for the *D. holocanthus* spine for which stress and strain can be calculated using equations described in the text.

Table 6. Comparison of mechanical properties of the spine calculated using the cylindrical beam model and the tapered circular beam model. Values are given as average ± standard deviation.

Mechanical Property	Uniform Beam	Tapered Beam
Maximum Tensile Stress (MPa)	612 ± 81	760 ± 286
Young's Modulus (GPa)	12.9 ± 3.2	11.1 ± 3.4
Strain at Maximum Stress (%)	4.8 ± 0.4	6.8 ± 1

6 Applications and Bioinspiration

Bioinspiration is field that aims to study designs in nature that have been developing for millions of years through evolution and use them to inspire human engineering applications. In recent years, bioinspiration has been gaining more attention. Scales in particular have been studied extensively because they help protect an animal while still maintaining flexibility and mobility. The erectile spines of the porcupine fish increase the size of the fish, making the fish difficult for predators to swallow, but allow the fish to become streamlined and smooth when not being attacked. These spines also serve to irritate the predator with their sharp tapered ends, while being lightweight allowing the porcupine fish to stay buoyant.

Many researchers who study spine structures argue that the design of the spines can be used for biomedical applications such as more efficient needles. However many of the spines studied, such as those of the stingray, bee, and cactus, have serrated or barbed edges . This design makes it easy for spines to penetrate the skin, but difficult to take out and are meant to inflict as much damage as possible to deter predators. While the spine of the porcupine fish does not have serrated edges, it is mean to pierce predators that attempt to eat it. Instead of studying it for needles, it may be more worthwhile to study the spines for their resistance to breaking as well as their ability to act as a deployable defense that can be compacted after use. In fact, porcupine fish spines have already been used for helmets in Polynesian island natives (Figure 35) to defend against weapons made of shark teeth [57].

Figure 35. Porcupine fish helmet worn by Gilbert and Ellice Island natives for defense in warfare [58].

7 Conclusion

This thesis explores the structure, composition, and mechanical properties of the porcupine fish spines from *D. holocanthus* and *D. hystrix* for the first time. There were no striking differences between the morphology of the spines of the two species. The main difference in between the two species is the size and number of spines on the fish. X-ray diffraction (XRD), energy dispersive X-ray spectroscopy (EDX), and thermogravimetric analysis (TGA) were used to determine the composition of the spine. Micro- and nano-computed tomography (CT), light microscopy, scanning electron microscopy (SEM), and transmission electron microscopy (TEM) were used to observe the macro- and microstructure of the spine. Mechanical properties were assessed using both nanoindentation and a cantilever test.

- The spines of both species were found to contain different ratios of mineral, protein, and water in different sections of the spine. The mineral component was identified as nanocrystalline hydroxyapatite with crystallite sizes of approximately 20 nm. Protein in the spine was found to likely be collagen from the banding structure seen in SEM as well as the fact that type I collagen is found in many other fish scales.
- The porcupine fish spine is a fairly complex structure, composed of multiple layers and intricate microstructure. Using μ- and nano-CT the structure of the spine was confirmed to have a spinous process, two lateral processes, and an axial process as mentioned in other literature. The spine is composed of five main layers: a protein core sheathed in a mineralized layer, a porous fibrous layer, an outer connective

tissue, and a layer of skin that is outside of the connective tissue. Transverse and longitudinal cross-sections show that the spine is made of sheets of connected fibers that are aligned longitudinally and radiate outward. In between these sheets are plies of fibers that are aligned radially. The microstructure of the spine most likely helps to prevent the spine from breaking by deflecting cracks that may propagate through the spine.

- Nanoindentation showed that the spine has a Young's modulus that ranges from 11 to 17 GPa and a hardness that ranges from 330 to 363 MPa depending on the section of the spine. Young's modulus and hardness were found to vary with location on the spine.
- Cantilever tests were performed and a mathematical model for a tapered beam was compared to a model using a uniform beam. The comparison showed that while the maximum stress between the two configurations was similar, the location of the maximum stress for the tapered beam is near the tip of the spine rather than at the spine base, which is the location of maximum stress for a uniform cross-section beam. This change in location may be beneficial for the fish so that if a spine breaks, it breaks at the tip and the fish doesn't have to regrow a whole spine, which is energy intensive.

Revisiting the hypothesis of this thesis, it was found that the spines were composed of hydroxyapatite and protein that is most likely collagen, which is what is found in other fish scales. The The tapered morphology of the spine did not improve the mechanical properties of the spine, but it changed the location of the maximum stress, making it easier for the fish to conserve resources in the situation that its spine does break.

The microstructure of the spine was shown to prevent crack propagation, which improves the toughness of the spines.

7.1 Recommendations for Future Research

Since this work is only a first foray into the structure of the porcupine fish spine, there is a lot more to understand about the structure and how it relates to the mechanical properties of the spine. Future work includes:

- Confirming that the fibers found in the spine are collagen.
- A full histological analysis, which can identify the presence of other proteins as well as cells to confirm the growth front of the spines.
- TEM of demineralized spines, which can help provide insight on the microstructure of the spine and the alignment of the fibers, confirming what was described in this thesis.
- Compression tests to understand the buckling behavior of the spines.
- Development of a more detailed mechanical model to describe mechanical behavior of the spine.

Appendix

Appendix A. Derivation of Equations for a Uniform Circular Cross-section

Consider a cantilever beam with uniform circular cross-section as shown in Figure 32. The moment at any location when there is a point load at the end of the cantilever beam is given by

$$\mathrm{M(x)} = -\mathrm{P(L-x)} \tag{A1}$$

where M is the moment at position x, L is the length of the beam, and P is the point load at the end of the beam. Using the moment curvature relation, where E is elastic modulus, v is vertical deflection, and I is second moment of inertia,

$$-\mathrm{M(x)} = \mathrm{EI}\frac{\mathrm{d^2v(x)}}{\mathrm{dx^2}} \tag{A2}$$

$$\Rightarrow \frac{\mathrm{d^2v(x)}}{\mathrm{dx^2}} = \frac{-\mathrm{M(x)}}{\mathrm{EI}} = \frac{\mathrm{P(L-x)}}{\mathrm{EI}}$$

*I*ntegrating twice, the resulting expression is

$$v(x) = \iint \frac{P(L-x)}{EI}\,dx\,dx = \frac{1}{EI}\left(\frac{-Px^3}{6} + \frac{PLx^2}{2} + C_1x + C_2\right)$$

with constants C_1 and C_2. Using the following boundary conditions:

$$\begin{cases} v(0) = 0 \Longrightarrow C_2 = 0 \\ \dfrac{dv(0)}{dx} = 0 \Longrightarrow C_1 = 0 \end{cases}$$

The equation for vertical deflection can then be simplified to

$$v(x) = \frac{P}{EI}\left(\frac{-1}{6}x^3 + \frac{1}{2}Lx^2\right) \tag{A3}$$

Since experiments only give measurements for the end deflection of the beam where $x = L$, maximum deflection v_{max} is

$$v_{max} = v(L) = \frac{P}{EI}\left(\frac{-1}{6}L^3 + \frac{1}{2}L \cdot L^2\right)$$

Therefore the expression for v_{max} is

$$v_{max} = \frac{PL^3}{3EI} \tag{A4}$$

The second moment of area *I* for a circular cross-section is

$$I = \frac{\pi d^4}{64} \tag{A5}$$

Substituting, the second moment of area and rearranging the expression for v_{max},

$$E = \frac{64PL^3}{3\pi v_{max} d^4} \tag{A6}$$

Stress across the beam can be described using the following equation

$$\sigma(x, y) = -\frac{M(x)y}{I} \tag{A7}$$

Since the porcupine fish spine is mostly mineral, it is expected to fail under tension rather than compression. Therefore, the maximum flexural stress of a cantilever beam is the tensile stress on the top surface of the spine and is given by

$$\sigma_{max} = \frac{M_{max} y_{max}}{I} \tag{A8}$$

In the case of failure under tension, the neutral axis is at $y = 0$ for a circular cross-section, which means that for the maximum stress, $y_{max} = \frac{d}{2}$. Maximum stress across the beam is

at $x = 0$ so that $M_{max} = PL$. Substituting the second moment of inertia for a circular cross-section and the value for x and y into the expression for the maximum stress results in the following equation

$$\sigma_{max} = \frac{32\ PL}{\pi\ d^3} \tag{A9}$$

As part of Euler-Bernoulli bending theory, it is assumed that plane sections remain plane. Therefore, strain at maximum tensile stress ε_{max} is the maximum stress divided by the elastic modulus

$$\varepsilon_{max} = \frac{\sigma_{max}}{E} = \frac{3v_{max}d}{2L^2} \tag{A10}$$

Appendix B. Derivation of Mechanical Property Equations for a Tapered Beam with Circular Cross-Section

Referring to the diagram shown in Figure 32, the expression for strain energy (U) is used

$$U = \int_0^L \frac{M^2(x)}{2E\, I(x)}\, dx \tag{A10}$$

where $M(x) = -P(L - x)$ and I is the second moment of area of the beam, which in this case is a function of x. For a tapered beam with a constant diameter change and circular cross-section with d_A smaller diameter at the end of the beam and d_B the larger diameter at the base of the beam,

$$I(x) = \frac{\pi {d_B}^4}{64}\left(1 + \frac{(\beta - 1)}{L}x\right)^4 \tag{A11}$$

where $\beta = d_A/d_B < 1$.We can simplify this to

$$I(x) = I_B\left(1 + \frac{(\beta - 1)}{L}x\right)^4 \tag{A12}$$

since I_B is the second moment of area of the end of the beam with diameter d_B.

The maximum displacement of the tip of the tapered beam v_{max} is given by Castigliano's Theorem

$$v_{max} = \frac{\partial U}{\partial P} = \frac{\partial}{\partial P}\int_0^L \frac{M^2(x)}{2E\, I(x)}\, dx = \int_0^L \frac{M(x)\frac{\partial M}{\partial P}}{E\, I(x)}\, dx \tag{A13}$$

Taking the derivative of $M(x)$ with respect to P

$$\frac{\partial M(x)}{\partial P} = -(L - x) \tag{A14}$$

Substituting (A12) and (A14) into (A13),

$$v_{max} = \int_0^L \frac{P(L-x)^2}{E\ I(x)} dx$$

$$= \frac{P}{E\ I_B} \int_0^L \left(\frac{L^2}{\left(1 + \frac{(\beta-1)}{L}x\right)^4} - \frac{2L\ x}{\left(1 + \frac{(\beta-1)}{L}x\right)^4} + \frac{x^2}{\left(1 + \frac{(\beta-1)}{L}x\right)^4} \right) dx$$

Using substitution, let

$$\left(1 + \frac{(\beta-1)}{L}x\right) = 1 + \alpha x = 1 + w$$

where,

$\alpha = \frac{(\beta-1)}{L}$ and $w = \alpha x \Rightarrow dw = \alpha dx$

With substitution, the range for integration is changed from $0 \rightarrow L$ to $0 \rightarrow (\beta - 1)$.

$$v_{max} = \frac{P}{E\ I_B} \int_0^{(\beta-1)} \left(\frac{L^2}{(1+w)^4} - \frac{2L\ x}{(1+w)^4} + \frac{x^2}{(1+w)^4} \right) \frac{1}{\alpha} dw$$

$$= \frac{P}{E\ I_B \alpha} \left(\frac{-L^2}{3(1+w)^3} + \frac{L}{3\alpha} \frac{(3w+1)}{(1+w)^3} - \frac{1}{3\alpha^2} \frac{(3\mathrm{w}^2 + \mathrm{w} + 1)}{(1+\mathrm{w})^3} \right) \Bigg|_0^{(\beta-1)}$$

$$= \frac{\mathrm{P}}{\mathrm{E\ I_B \alpha}} \left(\frac{-\mathrm{L}^2}{3\beta^3} + \frac{L^2}{3} + \frac{L}{3\alpha} \left(\frac{3\beta - 2}{\beta^3} - 1 \right) - \frac{1}{3\alpha^2} \left(\frac{(3(\beta-1)^2 + (\beta-1) + 1}{(1+w)^3} - 1 \right) \right)$$

Substituting α with $\frac{(\beta-1)}{L}$

$$v_{max} = \frac{PL}{E\ I_B(\beta-1)} \left(\frac{L^2(\beta-1)}{3\beta} \right) = \frac{PL^3}{3\beta E\ I_B} = \frac{64PL^3}{3\beta E \pi {d_B}^4}$$

From this, an expression for Young's modulus E is found

$$E = \frac{64\,P\,L^3}{3\pi\beta {d_B}^4 v_{max}} \tag{A15}$$

The maximum stress for the tapered beam can be derived using Equation (A7). While the moment on the beam stays the same, both *y* and *I* become functions of *x*, changing along the length of the beam. Assuming a linear change in diameter along the length of the spine, *y* can be represented as a function of the diameter of the beam cross-section *d*(*x*) divided by 2

$$d(x) = d_B + \frac{(d_A - d_B)}{L}x \tag{A16}$$

where d_A is the smallest diameter of the tapered beam, d_B is the largest diameter of the tapered beam, and L is the length of the beam. Let $d_A = \beta d_B$ so that Equation (A16) becomes

$$d(x) = d_B\left(1 + \frac{(\beta - 1)}{L}x\right) \tag{A17}$$

Equation (A17) can then be placed into expressions *y* (*x*) to yield

$$y(x) = \frac{d(x)}{2} = \frac{d_B}{2}\left(1 + \frac{(\beta - 1)}{L}x\right) \tag{A18}$$

Substituting Equations (A18) and (A11) into Equation (A7),

$$\sigma(x) = -\frac{M(x)y(x)}{I(x)} = -\frac{-P(L-x) * \frac{d_B}{2}\left(1 + \frac{(\beta - 1)}{L}x\right)}{\frac{\pi {d_B}^4}{64}\left(1 + \frac{(\beta - 1)}{L}x\right)^4}$$

which reduces to

$$\sigma(x) = \frac{32P(L-x)}{\pi {d_B}^3 \left(1 + \frac{(\beta-1)}{L}x\right)^3} \tag{A19}$$

In order to find σ_{max}, the roots for $\sigma(x)$ must be found by taking the derivative of $\sigma(x)$ with respect to *x* and setting it equal to 0

$$\frac{d\sigma(x)}{dx} = -\frac{32P}{\pi {d_B}^3 \left(1 + \frac{(\beta-1)}{L}x\right)^3} - \frac{96P(L-x)(\beta-1)}{\pi L {d_B}^3 \left(1 + \frac{(\beta-1)}{L}x\right)^4} = 0$$

Simplifying results, the following expression is found

$$\Rightarrow \frac{-32PL^3[-2x(\beta-1) + L(3\beta-2)]}{\pi {d_B}^3 (L + (\beta-1)x)^4} = 0$$

$$\Rightarrow (-2x(\beta-1) + L(3\beta-2)) = 0$$

$$\Rightarrow -2x(\beta-1) = -L(3\beta-2)$$

$$\Rightarrow x = \frac{L(3\beta-2)}{2(\beta-1)}$$

where $0 < \beta < 2/3$. Plugging the expression for *x* back into Equation (A19)

$$\sigma_{max} = \frac{32P\left(L - \frac{L(3\beta-2)}{2(\beta-1)}\right)}{\pi {d_B}^3 \left(1 + \frac{(\beta-1)}{L}\frac{L(3\beta-2)}{2(\beta-1)}\right)^3} = \frac{32PL\left(1 - \frac{(3\beta-2)}{2(\beta-1)}\right)}{\pi {d_B}^3 \left(1 + \frac{(3\beta-2)}{2}\right)^3}$$

Simplifying this expression, the following expression for maximum stress is found

$$\sigma_{max} = \frac{128PL}{27\pi {d_B}^3 \beta^2 (1-\beta)} \tag{A20}$$

where $0 < \beta < 2/3$.

The maximum tensile strain can be found using Equation (A9)

$$\varepsilon_{max} = \frac{128PL}{27\pi {d_B}^3 \beta^2 (1-\beta)} \frac{3\pi\beta {d_B}^4 v_{max}}{64\ P\ L^3}$$

Then

$$\varepsilon_{max} = \frac{2 d_B v_{max}}{9\beta(1-\beta)L^2} \tag{A20}$$

Appendix C. Nano-computed Tomography, Histology, and Transmission Electron Microscopy Sample Preparation Protocol

1. Rehydrate sample with deionizd (DI) water: Discard half of the post-fixative solution (50% isopropyl alcohol and DI water) and fill with add DI water. Place vial on agitator for 5 minutes. Repeat once. Replace vial contents with DI water and place vial on agitator for five minutes. Repeat last step again.
2. Submerse sample in 1% osmium tetroxide for at least 5 hours and place on agitator to ensure osmium tetroxide penetrates the spine. Make sure to perform this step in a fume hood.
3. Wash sample of osmium tetroxide by replacing liquid in vial with DI water, placing vial on agitator, and waiting five minutes between rinses. Repeat 5-6 times.
4. Acetone dehydration: Stepwise dehydrate the sample with 20%, 50%, 70%, 90%, and 100% ethanol for 10 minutes each. Submerse sample in 100% ethanol again for 10 minutes. Replace vial liquid with 50/50 ethanol and acetone solution and leave for 10 minutes. Repeat with 100% ethanol twice.
5. Embed sample in Spurrs resin by covering sample with 50/50 acetone and Spurrs resin and leave overnight on agitator. Repeat for 90/10 Spurrs to acetone mix and leave overnight on agitator. Cover sample with 100% Spurrs resin for three days and replace resin each day. Transfer sample to a small metal dish and cover sample with 100% Spurrs resin. Let sample cure in 60˚C oven for two days.

Appendix D. Critical Point Drying Protocol

Protocol is for operation of Autosamdri-815 critical point dryer (Tousimis, Rockville, MD, USA).

1. Sample must be stepwise dehydrated using 25%, 50%, 75%, 90% and 100% ethanol or isopropanol with DI water for 10 minutes each step. Ethanol is recommended.
2. Open valve of CO_2 gas tank.
3. Unscrew screws on metal cylinder and remove cylinder.
4. Fill bomb with enough ethanol/isopropanol to cover sample.
5. Turn on power and refasten the cylinder by screwing the screws in evenly so that there is even pressure on the cylinder.
6. Adjust purge timer based on size of sample and amount of ethanol/isopropanol in bomb. Timer numbers are in 5-minute increments. Set to level to 5 for a full chamber.
7. Press the “Cool” button and wait for the indicator on the temperature dial to drop to 0˚C. When the dial reads 0˚C, press the “Fill” button.
8. Machine will automatically step through “Purge,” “Heat,” “Bleed,” and “Vent” steps. During the “Purge” step, you should see vapor leaving the “Purge/Vent Exhaust.” If you cannot see vapor leaving, adjust the “Purge-Vent” knob until you see vapor leaving.
9. After all steps are over, wait for the pressure dial to fall to 0, before removing sample.
10. Turn off machine and close CO_2 tank.

Notes:

- If during the “Fill” step, liquid sprays out of the chamber, this means that the vacuum is not sealed. Press “Vent,” check that the O-ring is secure, and start over.
- During “Heat” step, pressure must be at least 1072 psi and temperature should be at least 31˚C for ethanol to sublimate.
- If machine lights are flashing wildly after the “Heat” step, press the “Bleed” button to continue the process.

Appendix E. Chemical Drying with Hexamethyldisilazane Protocol

1. Sample must be stepwise dehydrated using 25%, 50%, 75%, 90% and 100% ethanol or isopropanol with DI water for 10 minutes each step. Repeat step for 100% alcohol.
2. After alcohol dehydration, stepwise switch to hexamethyldisilazane (HMDS) using 25%, 50%, 75%, 90%, and 100% HMDS and isopropanol for 10 minutes each. Repeat step for 100% HMDS.
3. Pour enough HMDS to cover your sample and leave in fume hood to dry overnight. When liquid is gone from container, sample is ready to use.

Appendix F. Cantilever Sample Preparation Protocol

1. Spines were first stepwise rehydrated using the same method as described in Step 1 of Appendix C.
2. The spine base was then potted in epoxy by stabilizing the spine vertically with a bit of Play-Dough.
3. Potted spines were then removed from their containers. Epoxy was cut and sanded to have flat edges and cut to a size that fits in the mechanical tester.

Appendix G. Polishing Protocol

1. Embed samples in epoxy and leave overnight.
2. Cut samples to suitable cross-sections using a saw.
3. Using medium grit sandpaper (1200 grit) on a rotating lap, smooth the edges of the sample so that there are no ridges on the sample and so that the sides are square with each other and opposite surfaces are parallel. This is so that your sample will lie flat when being imaged.
4. After using the lap, rinse sample in DI water and use compressed air to blow off grit or particles.
5. Using a finer grit sand paper (2400 grit), sand the sample back and forth in one direction. Use a microscope to check that all of the large scratches have been sanded away. Rinse sample with DI water and put into sonicator for 5 minutes to remove excess particles. Use compressed air to dry.
6. Using 3μm aluminum oxide polishing liquid and the corresponding polishing pad, Polish sample perpendicular to the direction from the last step. Once you see no scratches in the previously sanded direction, sonicate for another 5 minutes to remove excess particles.
7. Use the 0.05μm diamond polishing media with the corresponding polishing pad to polish samples. Polish in circular directions until scratches from the previous step have disappeared. Sonicate sample for 5 minutes and dry with compressed air.

References

1. Su, X., S. Kamat, and A.H. Heuer, *The structure of sea urchin spines, large biogenic single crystals of calcite.* Journal of Materials Science, 2000. **35**(22): p. 5545-5551.

2. Peterson, J., *Pterois volitans*. 2006: Wikipedia.

3. Pedroso, C.M., C. Jared, P. Charvet-Almeida, M.P. Almeida, D.G. Neto, M.S. Lira, V. Haddad, and K.C. Barbaro, *Morphological characterization of the venom secretory epidermal cells in the stinger of marine and freshwater stingrays.* Toxicon, 2007. **50**(5): p. 688-697.

4. Tonge, S.J., *Hystrix cristata, crested porcupine*. 2014: CalPhotos.

5. Tonge, S.J., *Tachyglossus aculeatus setosus, tasmanian echidna*. 2013: CalPhotos.

6. Rignanese, L., *Opuntia ficus-indica; indian-fig*. 2005.

7. Zhao, Z.-L., T. Shu, and X.-Q. Feng, *Study of biomechanical, anatomical, and physiological properties of scorpion stingers for developing biomimetic materials.* Materials Science and Engineering: C, 2016. **58**: p. 1112-1121.

8. Zhao, Z.-L., H.-P. Zhao, G.-J. Ma, C.-W. Wu, K. Yang, and X.-Q. Feng, *Structures, properties, and functions of the stings of honey bees and paper wasps: A comparative study.* Biology open, 2015: p. bio. 012195.

9. Moureaux, C., A. Perez-Huerta, P. Compere, W. Zhu, T. Leloup, M. Cusack, and P. Dubois, *Structure, composition and mechanical relations to function in sea urchin spine.* Journal of Structural Biology, 2010. **170**(1): p. 41-49.

10. Berman, A., L. Addadi, Å. Kvick, L. Leiserowitz, M. Nelson, and S. Weiner, *Intercalation of sea urchin proteins in calcite: Study of a crystalline composite material.* Science, 1990. **250**(4981): p. 664-667.

11. Halstead, B.W., M.J. Chitwood, and F.R. Modglin, *The anatomy of the venom apparatus of the zebrafish, pterois-volitans (linnaeus).* Anatomical Record, 1955. **122**(3): p. 317-334.

12. Bowes, J.H. and M.M. Murray, *The chemical composition of teeth: The composition of human enamel and dentine.* Biochemical Journal, 1935. **29**(12): p. 2721.

13. Bassett, H., *Lvi.—the phosphates of calcium. Part iv. The basic phosphates.* Journal of the Chemical Society, Transactions, 1917. **111**: p. 620-642.

14. Halstead, B.W. and F.R. Modglin, *A preliminary report on the venom apparatus of the bat-ray, holorhinus californicus.* Copeia, 1950. **1950**(3): p. 165-175.

15. Ocampo, R.R., B.W. Halstead, and F.R. Modglin, *The microscopic anatomy of the caudal appendage of the spotted eagleray, aëtobatus narinari (euphrasen), with special reference to the venom apparatus.* The Anatomical Record, 1953. **115**(1): p. 87-99.

16. Martin, T., J. Marugan-Lobon, R. Vullo, H. Martin-Abad, Z.-X. Luo, and A.D. Buscalioni, *A cretaceous eutriconodont and integument evolution in early mammals.* Nature, 2015. **526**(7573): p. 380-384.

17. Vincent, J.F.V. and P. Owers, *Mechanical design of hedgehog spines and porcupine quills.* Journal of Zoology, 1986. **210**: p. 55-75.

18. Malainine, M.E., A. Dufresne, D. Dupeyre, M. Mahrouz, R. Vuong, and M.R. Vignon, *Structure and morphology of cladodes and spines of opuntia ficus-indica. Cellulose extraction and characterisation.* Carbohydrate Polymers, 2003. **51**(1): p. 77-83.

19. Gindl-Altmutter, W. and J. Keckes, *The structure and mechanical properties of spines from the cactus opuntia ficus-indica.* Bioresources, 2012. **7**(1): p. 1232-1237.

20. Currey, J.D., *Comparison of strength of echinoderm spines and mollusk shells.* Journal of the Marine Biological Association of the United Kingdom, 1975. **55**(2): p. 419-424.

21. McKittrick, J., P.-Y. Chen, S. Bodde, W. Yang, E. Novitskaya, and M. Meyers, *The structure, functions, and mechanical properties of keratin.* Jom, 2012. **64**(4): p. 449-468.

22. Huang, F. and W. Guo, *Structural and mechanical properties of the spines from echinocactus grusonii cactus.* Journal of Materials Science, 2013. **48**(16): p. 5420-5428.

23. Chen, P.-Y., E. Novitskaya, C.-Y. Sun, J. McKittrick, and M.I. Lopez, *Toward a better understanding of mineral microstructure in bony tissues.* Bioinspired, Biomimetic and Nanobiomaterials, 2014. **3**(2): p. 71-84.

24. Santini, F., L. Sorenson, and M.E. Alfaro, *A new phylogeny of tetraodontiform fishes (tetraodontiformes, acanthomorpha) based on 22 loci.* Molecular Phylogenetics and Evolution, 2013. **69**(1): p. 177-187.

25. Leis, J.M., *Systematics and zoogeography of porcupinefishes (diodon, diodontidae, tetraodontiformes), with comments on egg and larval development.* Fishery Bulletin, 1978. **76**(3): p. 535-567.

26. Leis, J.M., *Nomenclature and distribution of the species of the porcupinefish family diodontidae (pisces, teleostei).* Memoirs of Museum Victoria, 2006. **63**(1): p. 77-90.

27. Pacific, A.o.t. *Balloonfish (spiny porcupine fish)*. 2015 [cited 2015 September 11, 2015]; Available from: http://www.aquariumofpacific.org/onlinelearningcenter/species/balloonfish.

28. Brainerd, E.L., *Pufferfish inflation - functional-morphology of postcranial structures in diodon holocanthus (tetraodontiformes).* Journal of Morphology, 1994. **220**(3): p. 243-261.

29. Wainwright, P.C. and R.G. Turingan, *Evolution of pufferfish inflation behavior.* Evolution, 1997. **51**(2): p. 506-518.

30. Breder, C.M. and E. Clark, *A contribution to the visceral anatomy, development, and relationships of the plectognathi. Bulletin of the amnh; v. 88, article 5.* 1947.

31. Winterbottom, R., *The familial phylogeny of the tetraodontiformes (acanthopterygii: Pisces): As evidenced by their comparative myology*. 1974: Smithsonian Institution Press.

32. Mills, A. and R. Passmore, *Pelagic paralysis.* The Lancet, 1988. **331**(8578): p. 161-164.

33. Simpson, L.L., *Neuropoisons: Their Pathophysiological Actions*. 2012: Springer Science & Business Media.

34. Brown, M.S. and H.S. Mosher, *Tarichatoxin - isolation and purification.* Science, 1963. **140**(356): p. 295-&.

35. Kao, C.Y., *Tetrodotoxin saxitoxin and their significance in study of excitation phenomena.* Pharmacological Reviews, 1966. **18**(2): p. 997-&.

36. Mines, D., S. Stahmer, and S.M. Shepherd, *Poisonings: Food, fish, shellfish.* Emergency Medicine Clinics of North America, 1997. **15**(1): p. 157-177.

37. Sugita, H., J. Iwata, C. Miyajima, T. Kubo, T. Noguchi, K. Hashimoto, and Y. Deguchi, *Changes in microflora of a puffer fish fugu niphobles, with different water temperatures.* Marine Biology, 1989. **101**(3): p. 299-304.

38. Narita, H., S. Matsubara, N. Miwa, S. Akahane, M. Murakami, T. Goto, M. Nara, T. Noguchi, T. Saito, and Y. Shida, *Vibrio alginolyticus, a ttx-producing bacterium isolated from the starfish astropecten polyacanthus.* Nippon Suisan Gakkaishi, 1987. **53**(4): p. 617-621.

39. Trevett, A.J., B. Mavo, and D.A. Warrell, *Tetrodotoxic poisoning from ingestion of a porcupine fish (diodon hystrix) in papua new guinea: Nerve conduction studies.* American Journal of Tropical Medicine and Hygiene, 1997. **56**(1): p. 30-32.

40. Song, H., C.L. Lu, L. Kang, L. Xie, Y.Y. Zhang, X.B. Zhou, and S. Zhong, *Tetrodotoxin alleviates acute heroin withdrawal syndrome: A multicentre, randomized, double‐blind, placebo‐controlled study.* Clinical and Experimental Pharmacology and Physiology, 2011. **38**(8): p. 510-514.

41. Byeon, M.S., J.Y. Park, S.W. Yoon, and H.W. Kang, *Structure and development of spines over the skin surface of the river puffer takifugu obscurus (tetraodontidae, teleostei) during larval growth.* Journal of Applied Ichthyology, 2011. **27**(1): p. 67-72.

42. Mittal, A.K. and T.K. Banerjee, *Functional organization of skin of green-puffer fish tetraodon fluviatilis (ham-buch) (tetraodontidae, pisces).* Zoomorphologie, 1976. **84**(2): p. 195-209.

43. Hertwig, I., H. Eichelberg, and J. Hentschel, *Light and electron-microscopic studies of the skin of the palembang puffer, tetraodon-steindachneri (teleostei, tetraodontidae).* Zoomorphology, 1992. **111**(4): p. 193-205.

44. Ehrlich, H., *Biological Materials of Marine Origin: Vertebrates*. Biologically-Inspired Systems, ed. S.N. Gorb. Vol. 4. 2015: Springer.

45. Zylberberg, L., J. Bonaventure, L. Cohensolal, D.J. Hartmann, and J. Bereiterhahn, *Organization and characterization of fibrillar collagens in fish scales insitu and invitro.* Journal of Cell Science, 1992. **103**: p. 273-285.

46. Sire, J.Y., P.C.J. Donoghue, and M.K. Vickaryous, *Origin and evolution of the integumentary skeleton in non-tetrapod vertebrates.* Journal of Anatomy, 2009. **214**(4): p. 409-440.

47. Bigi, A., A. Ripamonti, G. Cojazzi, G. Pizzuto, N. Roveri, and M.H.J. Koch, *Structural-analysis of turkey tendon collagen upon removal of the inorganic phase.* International Journal of Biological Macromolecules, 1991. **13**(2): p. 110-114.

48. Castania, V.A., J.W.S. Silveira, A.C. Issy, D.L. Pitol, M.L. Castania, A.D. Neto, E.A. Del Bel, and H.L.A. Defino, *Advantages of a combined method of decalcification compared to edta.* Microscopy research and technique, 2015. **78**(2): p. 111-118.

49. Oliver, W.C. and G.M. Pharr, *An improved technique for determining hardness and elastic-modulus using load and displacement sensing indentation experiments.* Journal of Materials Research, 1992. **7**(6): p. 1564-1583.

50. Danilchenko, S., O. Kukharenko, C. Moseke, I.Y. Protsenko, L. Sukhodub, and B. Sulkio-Cleff, *Determination of the bone mineral crystallite size and lattice strain from diffraction line broadening.* Crystal Research and Technology, 2002. **37**(11): p. 1234-1240.

51. Janković, B., L. Kolar-Anić, I. Smičiklas, S. Dimović, and D. Aranđelović, *The non-isothermal thermogravimetric tests of animal bones combustion. Part. I. Kinetic analysis.* Thermochimica Acta, 2009. **495**(1): p. 129-138.

52. de Albuquerque, C.Q., A.S. Martins, N.D. Leite, J.N. de Araujo, and A.M. Ribeiro, *Age and growth of the queen triggerfish balistes vetula (tetraodontiformes, balistidae) of the central coast of brazil.* Brazilian Journal of Oceanography, 2011. **59**(3): p. 231-239.

53. Zylberberg, L. and G. Nicolas, *Ultrastructure of scales in a teleost (carassius-auratus l) after use of rapid freeze-fixation and freeze-substitution.* Cell and Tissue Research, 1982. **223**(2): p. 349-367.

54. Song, F., A.K. Soh, and Y.L. Bai, *Structural and mechanical properties of the organic matrix layers of nacre.* Biomaterials, 2003. **24**(20): p. 3623-3631.

55. Wegst, U.G.K., H. Bai, E. Saiz, A.P. Tomsia, and R.O. Ritchie, *Bioinspired structural materials.* Nat Mater, 2014.

56. Nyman, J.S., A. Roy, X. Shen, R.L. Acuna, J.H. Tyler, and X. Wang, *The influence of water removal on the strength and toughness of cortical bone.* Journal of Biomechanics, 2006. **39**(5): p. 931-938.

57. Gudger, E.W., *Helmets from skins of the porcupine-fish.* Scientific Monthly, 1930. **30**: p. 432-442.

58. Museum, P.R., *Porcupine fish helmet*, in *Arms and Armour: Selected Objects from the Upper Gallery*, P.R. Museum, Editor.: http://web.prm.ox.ac.uk/weapons/index.php/tour-by-region/oceania/oceania/arms-and-armour-oceania-193/.